J. Fluid Mech. (2025), *vol.* 1021, A16, doi:10.1017/jfm.2025.10686

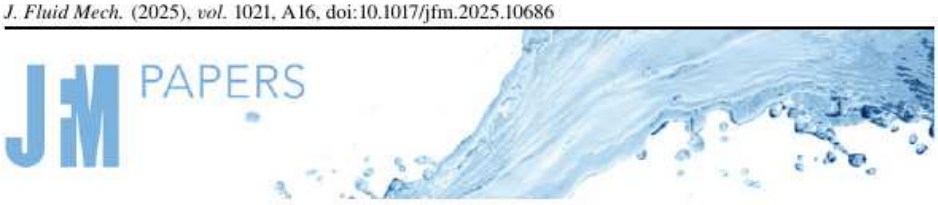

Effective flows across diffusio-phoretic membranes

Kevin Wittkowski[1], **Pier Giuseppe Ledda**[2], **Edoardo Carlo Giordano**[3], **François Gallaire**[1] **and Giuseppe Antonio Zampogna**[3]

[1]Laboratory of Fluid Mechanics and Instabilities, École Polytechnique Fédérale de Lausanne, Lausanne CH-1015, Switzerland

[2]Dipartimento di Ingegneria Civile, Ambientale e Architettura, Università degli Studi di Cagliari, Via Marengo 2, Cagliari 09123, Italy

[3]Dipartimento di Ingegneria Civile, Chimica e Ambientale, Università degli Studi di Genova, Via Montallegro 1, Genova 16145, Italy

Corresponding author: Giuseppe Antonio Zampogna, giuseppe.zampogna@unige.it

(Received 21 May 2025; revised 19 August 2025; accepted 1 September 2025)

Flows enabled by phoretic mechanisms are of significant interest in several biological and biomedical processes, such as bacterial motion and targeted drug delivery. Here, we develop a homogenisation-based macroscopic boundary condition that describes the effective flow across a diffusio-phoretic microstructured membrane, where the interaction between the membrane walls and the solute particles is modelled via a potential approach. We consider two cases where potential variations occur (i) at the pore scale and (ii) only in the close vicinity of the boundary, allowing for a simplified version of the macroscopic flow description, in the latter case. Chemical interactions at the microscale are rigorously upscaled to macroscopic phoretic solvent velocity and solute flux contributions, and added to the classical permeability and diffusivity properties of the membrane. These properties stem from the solution of Stokes advection–diffusion problems at the microscale, some of them forced by an interaction potential term. Eventually, we show an application of the macroscopic model to develop minimal phoretic pumps, showcasing its suitability for efficient design and optimisation procedures.

Key words: porous media, coupled diffusion and flow, microscale transport

1. Introduction

Flows induced by chemical and electrical interactions between solid boundaries and a surrounding fluid are frequently encountered in nature as well as in engineering

applications. Concentration gradients of different species can act as the driving force for chemical and biological transport. For example, bacteria motion is often induced by concentration differences (Adler 1975), while plants heavily rely on chemical gradients to ensure water and sugar transport (Bohr, Rademaker & Schulz 2018). Inspired by nature, artificial swimmers propel themselves by generating concentration gradients, e.g. through chemical reactions catalysed at their surface (Anderson 1989; Paxton *et al.* 2004; Palacci *et al.* 2013; Michelin *et al.* 2015; Brady 2021; Peng, Zhou & Brady 2022), so-called phoresis. Particles may self-propel thanks to asymmetric coatings on their surface. These exhibit initial directional self-motion, while at large times, random walk paths emerge (Howse *et al.* 2007). However, particles dispersed in colloidal dense suspensions can be effectively driven through concentration gradients, generating steady clusters (Theurkauff *et al.* 2012). In addition, temporal variations of the solute concentration can be exploited to drive particles' segregation and spatial patterns (Palacci *et al.* 2010). Conversely, concentration gradients at fixed boundaries can be employed to induce so-called phoretic flows. As an example, the retinal pigmental endothelium pump exploits concentration gradients to transport ions and molecules from the retina to the choroid and vice versa through the external layer of the vitreous, with the final result of draining excess fluid from the subretinal space (Sharma & Ehinger 2003; la Cour & Tezel 2005; Dvoriashyna *et al.* 2018, 2020).

Controlled flow manipulation at the microscale or nanoscale through minimal pumps recently found application also in microfluidics, including many applications in the field of biological analysis and screening (Whitesides 2006). Promising applications also include energy harvesting through the synergy of evaporation mechanisms with transport induced by electro-chemical interactions with nanopillar arrays, the so-called hydrovoltaic effect (Anwar & Tagliabue 2024), enabled by a concentration gradient of ions. Another example is the development of minimal phoretic pumps through the coating (the so-called phoretic layer to recall the interaction with the concentration gradient) of the inner walls of a microfluidic channel. Michelin & Lauga (2019) modelled the interaction with the phoretic layer as a non-zero surface tangential velocity, proportional to the concentration gradient along the normal direction through the so-called local phoretic mobility. Yu *et al.* (2020) employed similar phoretic-slip structures, for the same purpose. As a matter of fact, it has been shown that tailored phoretic membranes, fully permeable to the solute and composed of an array of microchannels or nanochannels, can effectively drive a flow through a concentration gradient across the structure (Lee *et al.* 2014). This approach would potentially circumvent technical challenges related to the fabrication of selective membranes based on size exclusion (Werber, Osuji & Elimelech 2016). Within this perspective, a rigorous derivation of the flow across fully permeable phoretic membranes can enhance predictability as well as promote efficient procedures for rational design, and eventually facilitate their deployment within different contexts.

A first theoretical framework for the description of diffusio-phoretic flows can be identified in Derjaguin *et al.* (1947). By leveraging hydrodynamic and thermodynamic considerations, the flux of a given chemical species in the vicinity of a phoretic surface depends on pressure and chemical potential differences. This result stems from a set of Stokes–Smoluchowski equations with a potential source term, which are nowadays the state of the art in the continuum modelling of these interfacial phenomena (Kirby 2010). The reactive materials employed in these phenomena often present intricate multi-scale structures involving pores (Yoshida *et al.* 2017; Herman & Segev 2024), pillars (Yu *et al.* 2020) and Janus coatings (Yang *et al.* 2016). The numerical description of these structures, likewise porous membranes (Chen *et al.* 2021) or porous nano-carriers (Li *et al.* 2022), may be prohibitive from a computational point of view, because of the large dispersion

of length and time scales within the same problem. In addition, results can be hardly generalised beyond the specific structure under consideration, and thus are of little use in industrial applications.

Several works develop simplified models valid at the scale of the whole membrane. The description of biological and engineered phoretic and osmotic flows typically employs *ad hoc* empirical laws whose foundations lie in the Spiegler–Kedem–Katchalsky equations (Kedem & Katchalsky 1958; Spiegler & Kedem 1966). These equations quantify the flow rates across the membrane via a linear combination of the contributions related to solvent pressure and solute concentration differences. These models are often developed for specific membrane geometries (Saffman 1960; Malone, Hutchinson & Prager 1974), or depend on empirical parameters (Koter 2006), with subsequent difficulties in the generalisation of these results and the necessity of finely tuned experimental measurements to estimate permeability, slip and equivalent diffusivities (Peeters *et al.* 1998).

More sophisticated attempts tried to upscale a molecular description to the whole structure scale (Cardoso & Cartwright 2014). Averaging techniques (Whitaker 1998) describe flows through reactive bulk porous media, based on Stokes–Smoluchowski equations containing a potential source term, valid within each pore (Wood, Quintard & Whitaker 2004; Veran, Aspa & Quintard 2009). Within this context, homogenisation theory is a suitable tool to describe flows through permeable structures such as porous media (Mei & Vernescu 2010) and microstructured boundaries (Jiménez Bolaños & Vernescu 2017). Recently, Zampogna & Gallaire (2020) introduced a homogenisation-based approach to quantify the flow across thin microstructured permeable membranes. The distinct separation between the macroscopic size of the membrane and the microscopic size of its microstructure enables a mathematical description that scales up the microscopic flow characteristics to the observable, macroscopic, level. Homogenisation theory thus establishes a rigorous connection between macroscale and microscale flows through microscale characteristic problems to determine permeability and filtration properties. This methodology has been used to describe hydrodynamic flows coupled with passive chemical transport in microstructured membranes, assuming negligible inertia within pores (Zampogna *et al.* 2022, 2023). The predictive accuracy of homogenisation theory for thin membranes was also tested in Ledda *et al.* (2021), who presented an approach to optimise flows through microstructured membranes. In these works, the hydrodynamic flow for the solvent equation obeys a stress-jump condition where the velocities at each side of the membrane are proportional to the stresses acting on the membrane, at the macroscopic scale. Similarly, the concentration field presents a flux-jump due to the chemical interactions with the microstructure. However, these models still lack the coupling between the hydrodynamic flow and active chemical transport at the solute–solvent–solid wall boundaries.

Here, we propose a homogenisation-based interface condition to describe flows through microstructured phoretic membranes, as depicted in figure 1(*a*). The outcome of the procedure, whose workflow is sketched in figure 1(*b*), is a macroscopic condition to be imposed on a thin homogeneous interface between two fluid regions (red smooth surface in figure 1*c*). This model also accounts for interactions with the solid boundaries that compose the microstructure, via an interaction potential that models the near-wall interactions driving the fluid motion through the pores of the membrane. To give a comprehensive view of the problem, we distinguish two cases: case (i) in which the interaction potential shows appreciable variations within the microscopic cell (so-called long-range potential), and case (ii) where the characteristic variation of the interaction potential is much smaller than the size of pores so that chemical interactions can be

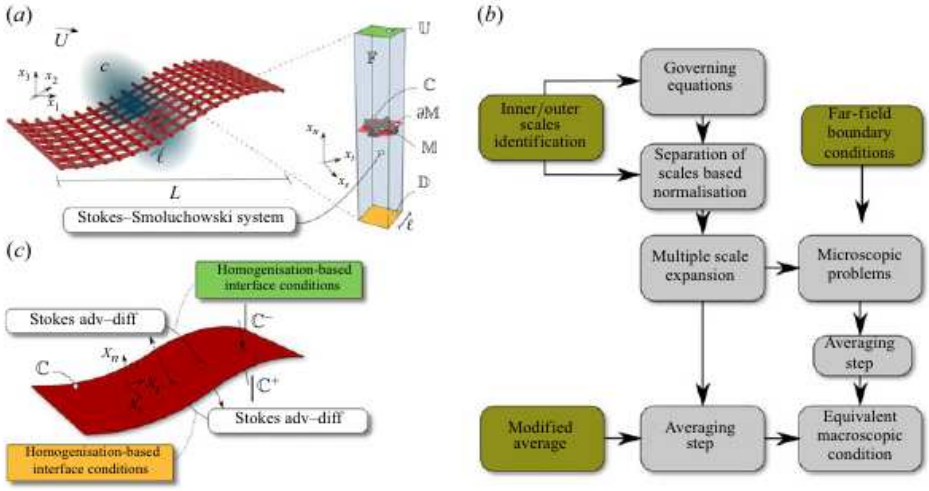

Figure 1. Fluid flow encountering a thin permeable membrane. The fluid is a two-component mixture of a solvent and a solute. (*a*) Real full-scale membrane realised by the periodic repetition of the microscopic cell represented on the right. A geometrical analysis of the membrane identifies two antipodal length scales: L represents the size of the whole membrane, while ℓ is the typical size of the microscopic periodic structure. (*b*) Diagram of the procedure used to deduce the macroscopic interface condition to describe interfacial flows through microstructured permeable walls, initially developed in Zampogna & Gallaire (2020). (*c*) From a macroscopic point of view the membrane, denoted with $\mathbb{C}$, corresponds to a fictitious interface between two bulk fluid regions, provided with a local frame of reference (X_s, X_t, X_n). We define the upward membrane side ($\mathbb{C}^-$) as the side of $\mathbb{C}$ whose outer normal coincides with X_n in the sketch, against that imposed on the downward opposite side ($\mathbb{C}^+$).

described as a boundary condition on the solid walls (so-called short-range potential). The paper is organised as follows. Section 2 presents the governing equations at the pore scale. Subsection 3.1 is devoted to the derivation of the homogenisation-based boundary condition, for the long-range potential case, whose microscale results are presented and validated within a macroscopic context in § 3.2. Section 4 is analogous to § 3, but focused on the short-range potential case; it shows how phoretic properties of membranes can tune the flow surrounding the membrane itself. The work is concluded with perspectives, limitations and possible next developments to overcome these limitations.

2. Phoretic flows near solid boundaries

We consider the viscous, incompressible flow through a microstructured membrane of a diluted solute of constant diffusivity D, transported by a Newtonian fluid of constant density ρ and dynamic viscosity μ (the solvent). The dimensional solute concentration (expressed in mol m^{-3}) and solvent flow fields (velocity and pressure) are denoted as $\hat{c}$ and $(\hat{u}_i, \hat{p})$, respectively. These quantities are defined within the fluid domain $\mathbb{F}$ (see figure 1), of characteristic length ℓ, while the size of the membrane is denoted as L. The ratio between these two quantities defines the separation of scales parameter $\epsilon = \ell/L \ll 1$. We introduce the non-dimensional interaction potential ϕ, modelling the chemical interactions between the solid boundaries and the solute, the Boltzmann constant k_b, the absolute temperature of the system T, and the Avogadro's number N_A. The Navier–Stokes equations are coupled with Fick's law for the conservation of the solute flux, and

both equations contain a potential source term. The set of governing equations reads

$$\rho\big(\hat{\partial}_\tau \hat{u}_i + \hat{u_j}\,\hat{\partial}_j \hat{u}_i\big) = -\,\hat{\partial}_i \hat{p} + \mu\,\hat{\partial}^2_{ll}\hat{u}_i - N_A \hat{c}\,\hat{\partial}_i \hat{\phi}, \quad \hat{\partial}_i \hat{u}_i = 0, \tag{2.1}$$

$$\hat{\partial}_\tau \hat{c} + \hat{\partial}_i \hat{F}_i = 0, \tag{2.2}$$

where $\hat{F}_i$ is the concentration flux

$$\hat{F}_i = \big(\hat{u}_i + \hat{u}_i^P\big)\hat{c} - D\,\hat{\partial}_i \hat{c} = \hat{u}_i \hat{c} + D\left(\frac{\hat{c}}{k_b \mathrm{T}}\hat{\partial}_i \hat{\phi} - \hat{\partial}_i \hat{c}\right), \tag{2.3}$$

and $\hat{u}_i^P = (D/k_b\mathrm{T})\,\hat{\partial}_i \hat{\phi}$ is the phoretic contribution to the velocity (Kirby 2010), where we assume the spatial dependency of the potential $\hat{\phi}$. To close the problem, the following boundary conditions are imposed on the membrane walls $\partial\mathbb{M}$:

$$\hat{u}_i = 0, \tag{2.4}$$

$$\hat{F}_i n_i^{\mathbb{M}} = \hat{S}_i n_i^{\mathbb{M}} \quad \text{on } \partial\mathbb{M}, \tag{2.5}$$

where S_i is a known source term describing the solute interactions with the solid walls, possibly spatially varying along the boundary $\partial\mathbb{M}$ itself. An $\hat{S}_i$ whose integral over $\partial\mathbb{M}$ is non-zero describes the production or absorption of a given solute species due to chemical reactions intervening at the membrane walls.

The interaction potential ϕ describes the interaction between surface, solvent and solute occurring at the molecular scale close to the solid boundaries of the membrane. Its range of action λ typically spans distances from 0.5 to 200 nm from the solid surface; see Wood *et al.* (2004) and Kirby (2010) for further details. In the short-range potential case ($\lambda \ll \ell$), Michelin & Lauga (2014) embedded the effects of ϕ on the fluid flow in a boundary condition for the velocity field on $\partial\mathbb{M}$. In the present work, we first consider the full equations (i.e. long-range potential case, $\lambda \approx \ell$), while the short-range potential equations ($\lambda \ll \ell$) are studied in § 4.

3. Homogenisation of the long-range potential equations

In this section, we apply the homogenisation procedure developed in Zampogna *et al.* (2023) to (2.1)–(2.5).

3.1. *Non-dimensionalisation of the flow equations*

We first analyse the problem close to the membrane (the inner problem), defined in a microscopic elementary cell sketched in figure 1(*a*). Variables in the microscopic domain are denoted by the superscript $\mathbb{I}$. The following non-dimensionalisation is employed:

$$\hat{\tau} = \frac{\ell}{U^{\mathbb{I}}}\tau, \quad \hat{c} = \Delta C^{\mathbb{I}}\, c^{\mathbb{I}}, \quad \hat{x} = \ell x,$$

$$\hat{p} = \Delta P^{\mathbb{I}}\, p^{\mathbb{I}} = N_A k_b \mathrm{T}\,\Delta C^{\mathbb{I}}\, p^{\mathbb{I}}, \quad \hat{\boldsymbol{u}} = U^{\mathbb{I}}\boldsymbol{u}^{\mathbb{I}} = \frac{\ell N_A k_b \mathrm{T}\,\Delta C^{\mathbb{I}}}{\mu}\boldsymbol{u}^{\mathbb{I}}. \tag{3.1}$$

Note that $\Delta P^{\mathbb{I}}$ is the pressure difference caused by the solute concentration gradient. The dimensionless system of equations close to the membrane thus reads

$$\begin{cases} Re_\ell \left(\partial_\tau u_i^{\mathbb{I}} + u_j^{\mathbb{I}}\, \partial_j u_i^{\mathbb{I}}\right) = -\partial_i p^{\mathbb{I}} + \partial_{ll}^2 u_i^{\mathbb{I}} - c^{\mathbb{I}}\, \partial_i \phi, \\ \partial_i u_i^{\mathbb{I}} = 0, \\ Pe_\ell\, \partial_\tau c^{\mathbb{I}} + \partial_i F_i^{\mathbb{I}} = 0, \\ F_i^{\mathbb{I}} = Pe_\ell\, u_i^{\mathbb{I}} c^{\mathbb{I}} - \left(\partial_i c^{\mathbb{I}} + c^{\mathbb{I}}\, \partial_i \phi\right), \\ u_i^{\mathbb{I}} = 0 \text{ on } \partial\mathbb{M}, \\ F_i n_i^{\mathbb{M}} = S_i n_i^{\mathbb{M}} \text{ on } \partial\mathbb{M}, \end{cases} \tag{3.2}$$

where $Re_\ell = \rho U^{\mathbb{I}} \ell/\mu$ and $Pe_\ell = U^{\mathbb{I}} \ell/D$ are the Reynolds number and Péclet number, both defined with the microscopic characteristic length ℓ. Following the procedure sketched in figure 1(*b*), the separation of scales allows us to introduce a fast (microscopic) and slow (macroscopic) variable through the decomposition $x_i \longrightarrow x_i + \epsilon X_i$. Accordingly, spatial derivatives are transformed following the chain rule $\partial_i \longrightarrow \partial_i + \epsilon \partial_I$, where the subscripts i and I respectively denote derivation with respect to x_i and X_i. The unknown variables are expanded in series:

$$f^{\mathbb{I}} = \sum_{n=0}^{+\infty} \epsilon^n\, f^{\mathbb{I},n}(\boldsymbol{x}, \boldsymbol{X}, \tau), \tag{3.3}$$

where $f^{\mathbb{I}}$ represents the unknown velocity, pressure and concentration fields, and $f^{\mathbb{I},n}$ denotes their nth order approximations in the series expansion. Substituting the space variable decomposition and the form (3.3) into (3.2), and collecting each order term in ϵ, at leading order, one obtains

$$\begin{cases} -\partial_i p^{\mathbb{I},0} + \partial_{ll}^2 u_i^{\mathbb{I},0} - c^{\mathbb{I},0}\, \partial_i \phi = 0, \\ \partial_i u_i^{\mathbb{I},0} = 0, \\ \partial_i F_i^{\mathbb{I},0} = 0, \\ F_i^{\mathbb{I},0} = \partial_i c^{\mathbb{I},0} + c^{\mathbb{I},0}\, \partial_i \phi, \\ u_i^{\mathbb{I},0} = 0 \text{ on } \partial\mathbb{M}, \\ F_i^{\mathbb{I},0} n_i^{\mathbb{M}} = S_i n_i^{\mathbb{M}} \text{ on } \partial\mathbb{M}, \end{cases} \tag{3.4}$$

where we assumed $Re_\ell = Pe_\ell = \mathcal{O}(\epsilon)$ and $Pe_\ell = \mathcal{O}(\epsilon)$, i.e. the flow inertia and advective transport are negligible. This assumption is reasonable for a large range of biological flows (Jensen *et al.* 2016; Dvoriashyna *et al.* 2018) and engineering applications (Lee *et al.* 2014).

Equations are solved within the microscopic domain sketched in figure 1(*a*), whose boundary conditions on $\mathbb{U}$ and $\mathbb{D}$ are the continuity of (i) solvent velocity and tractions, and (ii) solute concentration and flux:

$$\hat{u}_i^{in} = \hat{u}_i^{out}, \quad \hat{\Sigma}_{jk}^{in} n_k = \hat{\Sigma}_{jk}^{out} n_k, \quad \hat{c}^{in} = \hat{c}^{out}, \quad \hat{F}_i^{in} n_i = \hat{F}_i^{out} n_i, \tag{3.5}$$

with periodicity on the lateral sides of the unit cell. The superscript *out* denotes the outer region, while *in* denotes the inner region (cf. figure 1*a*).

For the outer problem, valid far from the membrane where the interaction potential effects can be neglected, we employ the following non-dimensionalisation of the Navier–Stokes equations:

$$\hat{\tau} = \frac{L}{U^{\mathbb{O}}} \tau^{\mathbb{O}}, \quad \hat{c} = \Delta C^{\mathbb{O}}\, c^{\mathbb{O}}, \quad \hat{x} = L x^{\mathbb{O}}, \quad \hat{p} = \Delta P^{\mathbb{O}}\, p^{\mathbb{O}}, \quad \hat{u}_i = U^{\mathbb{O}} u_i^{\mathbb{O}} = \frac{L\, \Delta P}{\mu} u_i^{\mathbb{O}}. \tag{3.6}$$

Once non-dimensionalised, the boundary conditions linking the microscopic and macroscopic fields on $\mathbb{U}$ and $\mathbb{D}$ read

$$u_i^{\mathbb{I},0} = u_i^{\mathbb{O},\mathbb{U}}, \quad \Sigma_{jk}^{\mathbb{I},0} n_k = \Sigma_{jk}^{\mathbb{O},\mathbb{U}} n_k, \quad F_i^{\mathbb{I},0} n_i = F_i^{\mathbb{O},\mathbb{U}} n_i \quad \text{on } \mathbb{U}, \tag{3.7}$$

$$u_i^{\mathbb{I},0} = u_i^{\mathbb{O},\mathbb{D}}, \quad \Sigma_{jk}^{\mathbb{I},0} n_k = \Sigma_{jk}^{\mathbb{O},\mathbb{D}} n_k, \quad F_i^{\mathbb{I},0} n_i = F_i^{\mathbb{O},\mathbb{D}} n_i \quad \text{on } \mathbb{D}. \tag{3.8}$$

In (3.7) and (3.8), superscripts $\mathbb{O}, \mathbb{U}$ or $\mathbb{O}, \mathbb{D}$ denote outer quantities evaluated on $\mathbb{U}$ or $\mathbb{D}$, respectively. Conditions (3.7) and (3.8) close the linear problem (3.4), whose formal solution is presented in the next subsubsection.

3.1.1. *Microscopic solution*

Since the problem is linear, we formally express the microscopic solution for the leading order flow approximation. We exploit the superposition principle for each source term in the governing equations (Zampogna & Gallaire 2020; Zampogna *et al.* 2022, 2023):

$$u_i^{\mathbb{I},0} = M_{ij} \Sigma_{jk}^{\mathbb{O},\mathbb{U}} n_k + N_{ij} \Sigma_{jk}^{\mathbb{O},\mathbb{D}} n_k + A_i F_k^{\mathbb{O},\mathbb{U}} n_k + B_i F_k^{\mathbb{O},\mathbb{D}} n_k + \alpha_i(\boldsymbol{S}), \tag{3.9}$$

$$p^{\mathbb{I},0} = Q_j \Sigma_{jk}^{\mathbb{O},\mathbb{U}} n_k + R_j \Sigma_{jk}^{\mathbb{O},\mathbb{D}} n_k + C F_k^{\mathbb{O},\mathbb{U}} n_k + D F_k^{\mathbb{O},\mathbb{D}} n_k + \beta(\boldsymbol{S}), \tag{3.10}$$

$$c^{\mathrm{I},0} = T F_k^{\mathbb{O},\mathbb{U}} n_k + Y F_k^{\mathbb{O},\mathbb{D}} n_k + \gamma(\boldsymbol{S}), \tag{3.11}$$

where M_{ij}, N_{ij}, A_j, B_j, α_i, Q_j, R_j, C, D, β, T, Y and γ are yet unknown quantities stemming from the linearity of the solution. Note that α_i, β and γ linearly depend on the boundary source term $\boldsymbol{S}$. We substitute (3.9)–(3.11) into the leading-order problem (3.4) and boundary condition (3.7), group terms by common forcings, and derive several sets of equations to be satisfied independently of the forcing values. Therefore, we obtain several problems for M_{ij}, N_{ij}, A_j, B_j, α_i, Q_j, R_j, C, D, β, T, Y and γ within the microscopic domain, presented now in detail. The problems below are written in the frame of reference of the membrane (x_s, x_t, x_n).

Tensors M_{ij} and N_{ij} and vectors Q_j and R_j stem from the pure hydrodynamic problem and satisfy two independent microscopic problems with the same structure of the Stokes equations, but forced by unitary stress at the far-field boundaries, i.e.

$$\begin{cases} -\partial_i Q_j + \partial_{ll}^2 M_{ij} = 0 \text{ in } \mathbb{F}, \\ \partial_i M_{ij} = 0 \text{ in } \mathbb{F}, \\ M_{ij} = 0 \text{ on } \partial\mathbb{M}, \\ \Sigma_{pq}(M_{\cdot j}, Q_j) n_q = \delta_{jp} \text{ on } \mathbb{U}, \\ \Sigma_{pq}(M_{\cdot j}, Q_j) n_q = 0 \text{ on } \mathbb{D}, \\ M_{ij},\ Q_j \text{ periodic along } \boldsymbol{t} \text{ and } \boldsymbol{s}, \end{cases} \quad \begin{cases} -\partial_i R_j + \partial_{ll}^2 N_{ij} = 0 \text{ in } \mathbb{F}, \\ \partial_i N_{ij} = 0 \text{ in } \mathbb{F}, \\ N_{ijk} = 0 \text{ on } \partial\mathbb{M}, \\ \Sigma_{pq}(N_{\cdot j}, R_j) n_q = 0 \text{ on } \mathbb{U}, \\ \Sigma_{pq}(N_{\cdot j}, R_j) n_q = \delta_{jp} \text{ on } \mathbb{D}, \\ N_{ij},\ R_j \text{ periodic along } \boldsymbol{t} \text{ and } \boldsymbol{s}. \end{cases} \tag{3.12}$$

Tensors M_{ij} and N_{ij} represent the tensors that relate the velocity through the membrane with the macroscopic stresses acting on each side of the membrane (Zampogna & Gallaire 2020). Similarly, the vectors Q_j and R_j relate the pressure field to the macroscopic stresses on each side of the membrane. The far-field conditions $\Sigma_{pq}(M_{\cdot j}, Q_j) n_q = \delta_{jp}$ on $\mathbb{U}$ and $\Sigma_{pq}(N_{\cdot j}, R_j) n_q = \delta_{jp}$ on $\mathbb{D}$ set the values of Q_j and R_j on $\mathbb{U}$ and $\mathbb{D}$, respectively, and ensure the well-posedness of problem (3.12).

Scalars T and Y satisfy two independent Smoluchowski microscopic problems describing the passive transport of the solute concentration, i.e.

$$\begin{cases} \partial_{ii}^2 T + \partial_i\phi\,\partial_i T + T\,\partial_{ii}^2\phi = 0 \text{ in } \mathbb{F} \\ (\partial_i T + T\,\partial_i\phi)n_i^{\mathbb{M}} = 0 \text{ on } \partial\mathbb{M} \\ -\partial_i T n_i = 1 \text{ on } \mathbb{U} \\ -\partial_i T n_i = 0 \text{ on } \mathbb{D} \\ T \text{ periodic along } \boldsymbol{t} \text{ and } \boldsymbol{s} \end{cases} \quad \begin{cases} \partial_{ii}^2 Y + \partial_i\phi\,\partial_i Y + Y\,\partial_{ii}^2\phi = 0 \text{ in } \mathbb{F} \\ (\partial_i Y + Y\,\partial_i\phi)n_i^{\mathbb{M}} = 0 \text{ on } \partial\mathbb{M} \\ -\partial_i Y n_i = 0 \text{ on } \mathbb{U} \\ -\partial_i Y n_i = 1 \text{ on } \mathbb{D} \\ Y \text{ periodic along } \boldsymbol{t} \text{ and } \boldsymbol{s}, \end{cases} \tag{3.13}$$

where $n_i^{\mathbb{M}}$ denotes the normal to $\partial\mathbb{M}$ pointing towards the fluid domain. Problems (3.13) relate the concentration field close to the membrane to the concentration fluxes in the normal membrane direction.

Other microscopic problems emerge from the coupling between the velocity and concentration fields through the interaction potential

$$\begin{cases} -\partial_i C + \partial_{ll}^2 A_i + T\,\partial_i\phi = 0 \text{ in } \mathbb{F} \\ \partial_i A_i = 0 \text{ in } \mathbb{F} \\ A_i = 0 \text{ on } \partial\mathbb{M} \\ \Sigma_{pq}(A_\cdot, C)n_q = 0 \text{ on } \mathbb{U} \text{ and } \mathbb{D} \\ A_i, C \text{ periodic along } \boldsymbol{t} \text{ and } \boldsymbol{s} \end{cases} \quad \begin{cases} -\partial_i D + \partial_{ll}^2 B_i + Y\,\partial_i\phi = 0 \text{ in } \mathbb{F} \\ \partial_i B_i = 0 \text{ in } \mathbb{F} \\ B_i = 0 \text{ on } \partial\mathbb{M} \\ \Sigma_{pq}(B_\cdot, D)n_q = 0 \text{ on } \mathbb{U} \text{ and } \mathbb{D} \\ B_i, D \text{ periodic along } \boldsymbol{t} \text{ and } \boldsymbol{s}, \end{cases} \tag{3.14}$$

where A_i, B_i, C, D quantify the velocity and pressure contributions induced by the concentration gradient within the fluid domain close to the membrane. The associated problems are formally analogous to the Stokes equations with homogeneous boundary conditions, but require the solution of (3.13) beforehand since the concentration-related volumetric terms in the momentum equations ($T\,\partial_i\phi$ and $Y\,\partial_i\phi$) act as sources.

The phoretic boundary contributions solve the coupled problems

$$\begin{cases} \partial_{ii}^2\gamma + \partial_i\phi\partial_i\gamma + \gamma\partial_{ii}^2\phi = 0 \text{ in } \mathbb{F} \\ (\partial_i\gamma + \gamma\partial_i\phi)n_i^{\mathbb{M}} = S_i n_i^{\mathbb{M}} \text{ on } \partial\mathbb{M} \\ -\partial_i\gamma n_i = 0 \text{ on } \mathbb{U} \text{ and } \mathbb{D} \\ \gamma \text{ periodic along } \boldsymbol{t} \text{ and } \boldsymbol{s} \end{cases} \quad \begin{cases} -\partial_i\beta + \partial_{ll}^2\alpha_i + \gamma\partial_i\phi = 0 \text{ in } \mathbb{F} \\ \partial_i\alpha_i = 0 \text{ in } \mathbb{F} \\ \alpha_i = 0 \text{ on } \partial\mathbb{M} \\ \Sigma_{pq}(\alpha_\cdot, \beta)n_q = 0 \text{ on } \mathbb{U} \text{ and } \mathbb{D} \\ \alpha_i, \beta \text{ periodic along } \boldsymbol{t} \text{ and } \boldsymbol{s}, \end{cases} \tag{3.15}$$

where β plays a role analogous to the pressure in the Stokes-like problem for α_i. The boundary condition on $\partial\mathbb{M}$ in the problem for γ contains the source term $S_i = S_i(\boldsymbol{x})$. Quantity γ is the phoretic contribution to $c^{\mathrm{I},0}$ and acts as a source term for the concentration field. Vector α_i instead represents the phoretic membrane velocity contribution purely induced by concentration differences on $\partial\mathbb{M}$ due to the solute–membrane interactions embedded in γ.

Equations (3.9)–(3.11) with the solvability conditions (3.12)–(3.15) form a closed physico-chemical description of the transport across the membrane. However, the formal solution (3.9)–(3.11) to (3.4) depends on the fast and slow variables, while our final objective consists of developing purely macroscopic interface conditions valid on the homogeneous membrane $\mathbb{C}$ (cf. figure 1*c*). In the next subsection, we therefore perform an averaging step.

3.1.2. *From the microscopic solution to the macroscopic interface condition*

To filter the microscale dependence in (3.9)–(3.11), the upward $\bar{\cdot}^-$ and downward $\bar{\cdot}^+$ (surface) averages are introduced (Zampogna *et al.* 2023):

$$\bar{\cdot}^- = \lim_{x_n\to+\infty} \frac{1}{|\mathbb{U}|}\int_{\mathbb{U}} \cdot\,\mathrm{d}x_s\,\mathrm{d}x_t \quad \text{and} \quad \bar{\cdot}^+ = \lim_{x_n\to-\infty} \frac{1}{|\mathbb{D}|}\int_{\mathbb{D}} \cdot\,\mathrm{d}x_s\,\mathrm{d}x_t. \tag{3.16}$$

The introduction of upward and downward averages allows for discontinuous macroscopic velocity and concentration profiles across the membrane, which is crucial in the problem analysed here since the main fluid flow driving force is represented by microscopic variations in the solute concentration field. By applying averages (3.16) to (3.9)–(3.11), we obtain the following set of equations for the velocity and concentration field at the upward ($\mathbb{C}^-$) and downward ($\mathbb{C}^+$) sides of the membrane:

$$u_i^- := \overline{u^{\mathbb{I},0}}_i^- = \mathcal{M}_{ij}^- \Sigma_{jk}^{\mathbb{C}^-} n_k + \mathcal{N}_{ij}^- \Sigma_{jk}^{\mathbb{C}^+} n_k + \mathcal{A}_i^- F_k^{\mathbb{C}^-} n_k + \mathcal{B}_i^- F_k^{\mathbb{C}^+} n_k + \alpha_i^-(\boldsymbol{S}), \quad (3.17)$$

$$u_i^+ := \overline{u^{\mathbb{I},0}}_i^+ = \mathcal{M}_{ij}^+ \Sigma_{jk}^{\mathbb{C}^-} n_k + \mathcal{N}_{ij}^+ \Sigma_{jk}^{\mathbb{C}^+} n_k + \mathcal{A}_i^+ F_k^{\mathbb{C}^-} n_k + \mathcal{B}_i^+ F_k^{\mathbb{C}^+} n_k + \alpha_i^+(\boldsymbol{S}), \quad (3.18)$$

$$p^- := \overline{p^{\mathbb{I},0}}^- = \mathcal{Q}_j^- \Sigma_{jk}^{\mathbb{C}^-} n_k + \mathcal{R}_j^- \Sigma_{jk}^{\mathbb{C}^+} n_k + \mathcal{C}^- F_k^{\mathbb{C}^-} n_k + \mathcal{D}^- F_k^{\mathbb{C}^+} n_k + \beta^-(\boldsymbol{S}), \quad (3.19)$$

$$p^+ := \overline{p^{\mathbb{I},0}}^+ = \mathcal{Q}_j^+ \Sigma_{jk}^{\mathbb{C}^-} n_k + \mathcal{R}_j^+ \Sigma_{jk}^{\mathbb{C}^+} n_k + \mathcal{C}^+ F_k^{\mathbb{C}^-} n_k + \mathcal{D}^+ F_k^{\mathbb{C}^+} n_k + \beta^+(\boldsymbol{S}), \quad (3.20)$$

$$c^- := \overline{c^{\mathbb{I},0}}^- = \mathcal{T}^- F_k^{\mathbb{C}^-} n_k + \mathcal{Y}^+ F_k^{\mathbb{C}^+} n_k + \gamma^-(\boldsymbol{S}), \quad (3.21)$$

$$c^+ := \overline{c^{\mathbb{I},0}}^+ = \mathcal{T}^+ F_k^{\mathbb{C}^-} n_k + \mathcal{Y}^+ F_k^{\mathbb{C}^+} n_k + \gamma^+(\boldsymbol{S}), \quad (3.22)$$

where

$$\mathcal{M}_{ij}^- = \overline{M}_{ij}^- - x_n|_{\mathbb{U}} (\delta_{it}\delta_{jt} + \delta_{is}\delta_{js}), \quad \mathcal{M}_{ij}^+ = \overline{M}_{ij}^+, \quad \mathcal{Q}_{ij}^\pm = \overline{Q}_{ij}^\pm, \quad (3.23)$$

$$\mathcal{A}_i^\pm = \overline{A}_i^\pm, \quad \mathcal{B}_i^\pm = \overline{B}_i^\pm, \quad \mathcal{C}^\pm = \overline{C}^\pm, \quad \mathcal{D}^\pm = \overline{D}^\pm, \quad (3.24)$$

$$\mathcal{T}^- = \overline{T}^- - x_n|_{\mathbb{U}}, \quad \mathcal{T}^+ = \overline{T}^+,$$

$$\mathcal{N}_{ij}^- = \overline{N}_{ij}^-, \quad \mathcal{N}_{ij}^+ = \overline{N}_{ij}^+ - x_n|_{\mathbb{D}} (\delta_{it}\delta_{jt} + \delta_{is}\delta_{js}), \quad \mathcal{R}_{ij}^\pm = \overline{R}_{ij}^\pm,$$

$$\mathcal{Y}^- = \overline{Y}^-, \quad \mathcal{Y}^+ = \overline{Y}^+ - x_n|_{\mathbb{D}}, \quad (3.25)$$

$$\alpha_i^\pm = \overline{\alpha}_i^\pm, \quad \beta^\pm = \overline{\beta}^\pm, \quad \gamma^\pm = \overline{\gamma}^\pm, \quad (3.26)$$

represent the effective tensorial properties of the solvent–solute–membrane triplet. We notice that some components of the effective tensors are not calculated as the simple average (3.16) of the corresponding microscopic quantities, but require a further correction arising from the linearity of the microscopic far-field solution (for further details, cf. Zampogna *et al.* 2023). The velocity field at the membrane is given by several contributions. If only the first two terms on the right-hand sides in (3.17) and (3.18) are considered, then the problem reduces to a pure hydrodynamic problem governed by the Stokes equations across the membrane (Zampogna *et al.* 2023). In this case, the macroscopic velocity at one side of the membrane is proportional to the stresses at both sides of the membrane. The velocity in the normal membrane direction is reminiscent of the Darcy law, while the tangential velocity is governed by a Navier slip condition (Ledda *et al.* 2021). Therefore, these proportionality coefficients $\mathcal{M}_{ij}^\pm$ and $\mathcal{N}_{ij}^\pm$ are also called the upward and downward Navier tensors, where both permeability ($\mathcal{M}_{nn}^\pm$ and $\mathcal{N}_{nn}^\pm$) and slip ($\mathcal{M}_{tt}^\pm$, $\mathcal{M}_{ss}^\pm$, $\mathcal{N}_{tt}^\pm$ and $\mathcal{N}_{ss}^\pm$) terms appear.

Analogously, if we consider only the passive transport of a chemical species, then (3.21) and (3.22) describe the concentration jump at the membrane. Scalars $\mathcal{T}^\pm$ and $\mathcal{Y}^\pm$ represent the effective diffusivity of the solute in the normal membrane direction, deviating from the bulk one due to the membrane microstructure.

The coupling given by the interaction potential gives rise to several additional terms. The velocity field depends also on the concentration flux across the membrane due to the presence of the potential ϕ in the leading-order problem (3.4): vectors $\mathcal{A}_i^\pm$ and $\mathcal{B}_i^\pm$ indeed

represent the solute gradient effect on the solvent flow, and can be defined as the bulk fluid mobility across the membrane. Eventually, term $\alpha_i^{\pm}$ represents the surface phoretic velocity generated by the solute concentration variation at the solid walls of the membrane inclusions, and γ is an additional concentration stemming from the solute source at the membrane walls. We eventually note that due to the assumption of a diffusion-dominant transport process at the microscale ($Pe_\ell = \mathcal{O}(\epsilon)$), the equations for the solute concentration do not contain the source terms associated with the hydrodynamic problem, i.e. the upward and downward solvent stresses. To provide an easy-to-use version of (3.17)–(3.22), we drop the complex notations needed for their rigorous mathematical development, and we specialise them for the case of a two-dimensional membrane of local coordinates (t, n) with isotropic microstructure and source term S_i exhibiting a purely normal-to-the-membrane gradient. We focus only on the velocity and concentration solution since the pressure equations are not used in the macroscopic resolution (cf. Zampogna *et al.* 2023). In this case, (3.17)–(3.22) read

$$u_n^- = \mathcal{M}_{nn}^-(-p + \partial_n u_n)^- + \mathcal{N}_{nn}^-(-p + \partial_n u_n)^+ + \mathcal{A}_n^-\,\partial_n c^- + \mathcal{B}_n^-\,\partial_n c^+ + \alpha_n^-(\boldsymbol{S}), \tag{3.27}$$

$$u_t^- = \mathcal{M}_{tt}^-\frac{1}{2}(\partial_n u_t + \partial_t u_n)^- + \mathcal{N}_{tt}^-\frac{1}{2}(\partial_n u_t + \partial_t u_n)^+, \tag{3.28}$$

$$u_n^+ = u_n^- \tag{3.29}$$

$$u_t^+ = \mathcal{M}_{tt}^+\frac{1}{2}(\partial_n u_t + \partial_t u_n)^- + \mathcal{N}_{tt}^+\frac{1}{2}(\partial_n u_t + \partial_t u_n)^+, \tag{3.30}$$

$$c^- = \mathcal{T}^-\,\partial_n c^- + \mathcal{Y}^+\,\partial_n c^+ + \gamma^-(\boldsymbol{S}), \tag{3.31}$$

$$c^+ = \mathcal{T}^+\,\partial_n c^- + \mathcal{Y}^+\,\partial_n c^+ + \gamma^+(\boldsymbol{S}), \tag{3.32}$$

where the superscripts denote the upward (+) and downward (−) membrane sides, and the subscripts t and n denote tangential and normal derivatives.

3.2. *Solution and validation*

In this subsection, we compare our homogenised interface condition against full-scale cases. The equations found in § 3.1 are solved numerically within their respective domains using their weak-form implementation in the finite-element solver Comsol Multiphysics. Spatial discretisation is based on Taylor–Hood (P2-P1) triangular elements for solvent-related equations, and P2 triangular elements for the solute-related equations. The spatial convergence of the solution has been tested and is reported in Appendix A. We consider a two-dimensional phoretic membrane composed of an array of circular inclusions. The membrane located at the center of a U-shaped channel divides it into two parts. The membrane releases solute particles at an imposed rate $\boldsymbol{S}(\boldsymbol{x})$ (cf. problem (3.15)), inducing a concentration gradient that drives the flow within the channel. A thorough review of typical potential functions for specific colloid-surface interactions can be found in Elimelech *et al.* (1995). Following Gebäck & Heintz (2019), we employ the potential ϕ defined as

$$\phi(\boldsymbol{x}) = \frac{\mathfrak{A}}{2}\left(1 - \tanh\left(\frac{d(\boldsymbol{x}) - a}{\delta'}\right)\right), \tag{3.33}$$

where $d(x)$ is the distance function from the centre of the solid inclusion of radius a. The parameters $\mathfrak{A}$ and δ' represent the amplitude and range of action of the interaction potential ϕ. When δ' is larger than the pore size, the structure is impermeable to the solute.

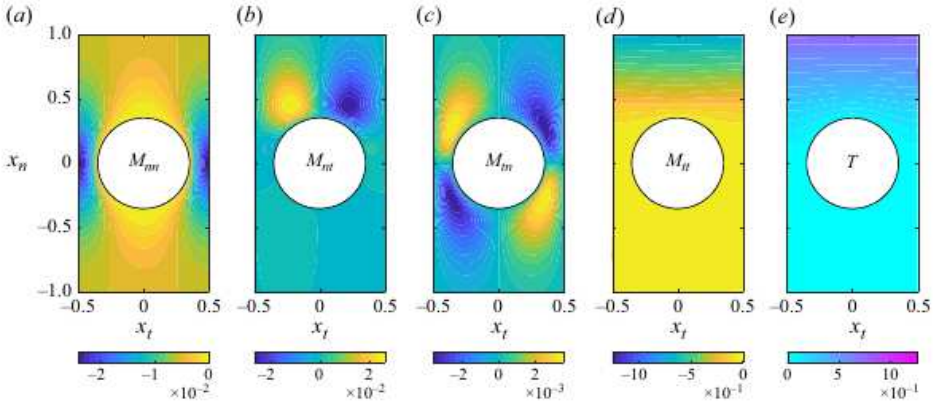

Figure 2. Microscopic fluid flow-related M_{ij} and concentration-related T fields arising from the solvent-to-solute interactions. These fields are not influenced by the source term $\boldsymbol{S}$. Since $N_{ij}(x_i) = -M_{ij}(-x_i)$ and $Y(x_i) = -T(-x_i)$ for symmetric geometries, these fields are not shown.

The amplitude $\mathfrak{A}$ instead quantifies the intensity of the solute membrane interaction. Given a solute particle at a distance $r < \delta'$ from the membrane, a larger $\mathfrak{A}$ implies a greater drift of the solute particles. In our case, $\mathfrak{A} = 10$ and $\delta' = \lambda/(1-a) = 0.0025$. These parameters' values fall in the range considered by Gebäck & Heintz (2019). The source term $\boldsymbol{S}$ in the solute flux specified in (2.5) is parametrised using an angle θ that expresses a rotation of the source S_i to the axis x_n as follows:

$$\boldsymbol{S}(\theta) = C_0(\boldsymbol{e}_n + \boldsymbol{e}_t) + \cos(\theta)\,\boldsymbol{e}_n + \sin(\theta)\,\boldsymbol{e}_t, \tag{3.34}$$

where $C_0 > 0$ is a constant value that ensures physical, positive concentrations. For example, if $\theta = 0$, then S_i is directed along x_n. Conversely, if $\theta = \pi/2$, then S_i is directed along x_t. This simple form allows one to appreciate the effects of the source orientation on the microscopic and macroscopic flow.

3.2.1. *Microscopic solution*

We present the solution of problems (3.12)–(3.15) obtained in § 3.1. We initially focus on the case of a solute release along the normal membrane direction, i.e. $\theta = 0$ in (3.34). Additionally, in the same equation, we specify $C_0 = 5$ in $\Delta C^{\mathbb{I}}/\ell$ units. Consequently, we avoid unphysical negative values of solute concentration. As already stated, these problems are defined within the microscopic elementary cell introduced in figure 1(*a*). Furthermore, microscopic spatial variables are denoted as (x_t, x_n).

Figure 2 depicts the iso-contours of M_{ij} and T. Because of the symmetry of the microscopic inclusion, N_{ij} and Y are not shown, i.e. $N_{ij}(x_k) = -M_{ij}(-x_k)$ and $Y(x_k) = -T(-x_k)$. In addition, the off-diagonal components of the upward Navier slip tensor M_{ij} are anti-symmetric (figure 2*b*,*c*). Components M_{nn} and M_{tn} resemble the Stokes flow velocity past a cylinder when the flow is driven by a pressure gradient. Conversely, M_{tt} and M_{nt} suggest the development of a linear profile of velocity due to tangential stress at the upper boundary. Iso-levels of T are shown in figure 2(*e*). Despite the local effect of the potential, there is a difference of one order of magnitude in T between the two sides of the solid inclusion.

Quantities A_i, α_i and γ are shown in figure 3. Vector B_i is not represented since $B_i(x_k) = -A_i(-x_k)$ for this symmetric configuration. A closer look into the microscopic

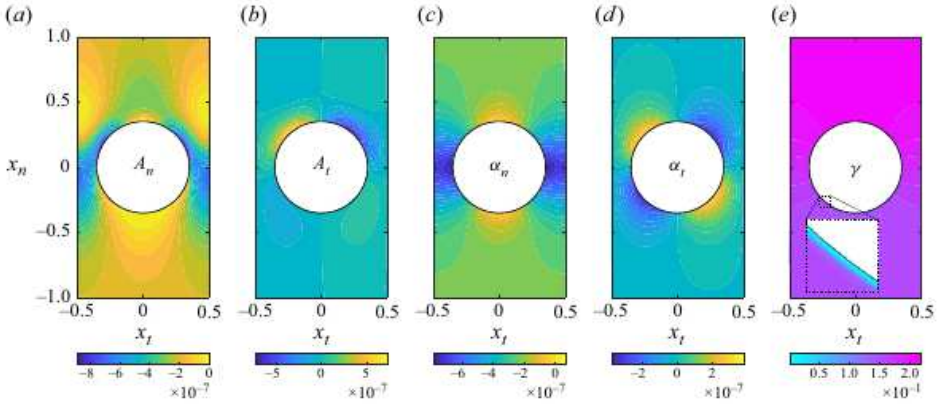

Figure 3. Microscopic fluid flow-related A_i, α_i and concentration-related γ fields arising from the solvent-to-solute interactions. The α_i, γ fields are influenced by the source term $\boldsymbol{S}$. In the present case, $\theta = 0$ and $C_0 = 5$. Since $A_i = -B_i$ for symmetric geometries, these fields are not shown.

A_n field (figure 3*a*) unveils the presence of the so-called plug flow velocity structure in the narrow region between two inclusions, typical of flows induced by osmotic or phoretic gradients where the fluid forcing has its maximum close to the walls (Kirby 2010). In the present case, this flow structure is associated with the gradient of T (which, in turn, can be linked to the microscopic solute transport). The tangential contribution A_t (figure 3*b*) is instead anti-symmetric due to the symmetry of the solid inclusion.

The normal-to-the-membrane component of α (figure 3*c*) exhibits a plug flow velocity profile. In analogy with $\boldsymbol{A}$, also the tangent component α_t is anti-symmetric (figure 3*d*). The plug flow distribution agrees with the interpretation of $\boldsymbol{\alpha}$, which is the solvent velocity contribution due to solute gradients induced by the solid walls, modelled here with the introduction of the release term S_i (cf. microscopic problem (3.15)). Eventually, the scalar field γ (figure 3*e*) represents an additional concentration stemming from solid–fluid interactions at the boundaries, which here highlights the anti-symmetry of the imposed flux S_i at the solid walls.

At this stage, the reader might wonder how S_i influences the microscopic flow and concentration structures. An intuitive answer is provided in figure 4(*a–c*), where the microscopic quantities influenced by S_i are reported, for $\theta = \pi/4$. The release term S_i influences γ, whose anti-symmetry axis is not aligned with x_n as in figure 3(*e*). Furthermore, flow structures associated with $\boldsymbol{\alpha}$ are rotated, leading to a net tangential-to-the-membrane velocity contribution due to α_t. All other microscopic quantities are not influenced by a rotation of $\boldsymbol{S}$ since they are not linked to the solute concentration gradients at the solid boundaries.

The microscopic solution fields are exploited to obtain their upward and downward averages (3.16). The non-zero entries of these quantities are listed in tables 1, 2 and 3. As already noticed in Zampogna *et al.* (2023), the upward and downward averages of M_{nn} (N_{nn}) are the same, due to the conservation of mass across the membrane, for normal stress forcing. This property is extended here also to A_n (B_n) and α_n since they contribute to the macroscopic normal-to-the-membrane velocity that must be conserved since there is no net flow rate at the solid boundary. A cross-comparison between tables 2 and 3 shows how a non-symmetric S_i produces a functional membrane anisotropy, quantified by a non-zero α_t.

	$\mathcal{M}_{tt}$	$\mathcal{M}_{nn}$	$\mathcal{N}_{tt}$	$\mathcal{N}_{nn}$	$\mathcal{T}$	$\mathcal{Y}$
,U	4.76×10^{-2}	4.98×10^{-3}	4.1×10^{-6}	-4.98×10^{-3}	1.20×10^{-2}	-1.07×10^{-3}
,D	4.1×10^{-6}	4.98×10^{-3}	4.76×10^{-2}	-4.98×10^{-3}	1.07×10^{-3}	-1.20×10^{-2}

Table 1. Non-zero averaged components of $\boldsymbol{M}$, $\boldsymbol{N}$, $\mathcal{T}$, $\mathcal{Y}$.

	γ	$\mathcal{A}_n$	$\mathcal{B}_n$	α_n
,U	2.13×10^{-1}	1.71×10^{-7}	-1.71×10^{-7}	-2.14×10^{-7}
,D	1.58×10^{-1}	1.71×10^{-7}	-1.71×10^{-7}	-2.14×10^{-7}

Table 2. Non-zero averaged components of γ, A, B, α for $\theta = 0$ in the source term of the microscopic problem (3.15) as defined in (3.34).

	γ	α_t	α_n
;U	5.31×10^{-2}	-6.19×10^{-5}	-3.63×10^{-5}
;D	6.69×10^{-2}	-6.19×10^{-5}	-3.63×10^{-5}

Table 3. Values of γ and α_i with $S_i(\boldsymbol{x})$ defined in (3.34) for $\theta = \pi/4$ and used in microscopic problem (3.15).

The effect of the concentration boundary forcing on α and γ is investigated through a parametric study for θ. The averaged values are sketched in figure 4(*d*,*e*) for $\theta \in [0, 2\pi]$. From these curves, one could *a priori* guess the membrane flow behaviour, independently of the macroscopic flow configuration. Assuming that the only driving force of the flow is the concentration gradient at the membrane walls (i.e. S_i), the dashed red lines suggest that for $\theta = \pi/2$ and $\theta = 3\pi/2$, the normal-to-the-membrane solvent velocity is zero, while the tangential one is maximum, thus denoting a pure tangential flow. Vice versa, for $\theta = 0$ and $\theta = 2\pi$, the solute gradient produces a pure normal-to-the-membrane flow. These indications suggest that homogenisation can provide macroscopic guidelines that can be included in a hypothetical design procedure. In the next subsection, we show how these microscopic averaged quantities influence the macroscopic behaviour of the flow across the membrane.

3.2.2. *Macroscopic solutions and comparison with full-scale simulations*

We compare the full-scale solution of (3.2) with the macroscopic solution obtained by replacing the full-scale membrane microstructure with a homogenised interface where conditions (3.17)–(3.22) apply. We consider the flow within the U-shaped two-dimensional channel sketched in figure 5. The channel upper left and upper right sides are open, and the fluid is free to flow across them. The duct is split in the middle by a phoretic membrane, whose microstructure is composed of an array of cylinders with a fluid-to-total ratio on the membrane centreline of 0.3. The microscopic membrane properties are varied to assess the capability of the model to catch anisotropic membrane behaviours. In the first configuration (figure 5), the membrane presents 10 solid inclusions ($\epsilon = 0.1$) and $\theta = 0$ in the source term S_i of (3.34). Figure 5 depicts the contours of the concentration field (magenta-to-cyan) for the full-scale (figure 5*a*) and macroscopic (figure 5*b*) solutions.

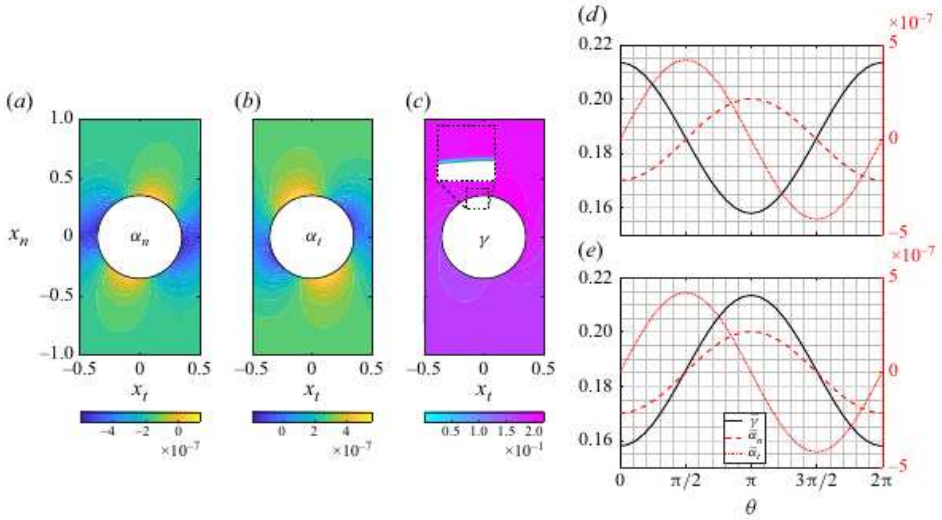

Figure 4. (*a*,*b*,*c*) Microscopic fluid flow-related α_i and concentration-related γ fields arising from the solute-to-solvent interactions. These fields are influenced by the source term S. In the present case, $\theta = \pi/4$. (*d*,*e*) Average γ and α_i values computed on the top (*d*) and bottom (*e*) sides of the solid inclusion as a function of the source rotation angle θ; see (3.34).

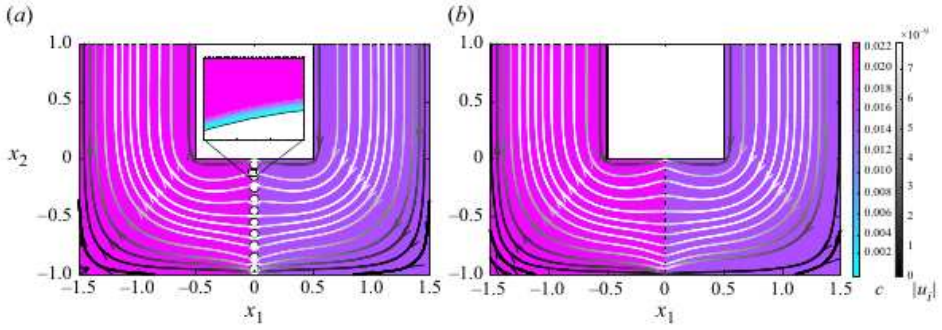

Figure 5. Comparison between the (*a*) full-scale and (*b*) macroscopic solutions in terms of solute concentration (iso-levels) and fluid flow velocity (streamlines coloured by velocity magnitude) in the U-shaped channel when $\theta = 0$ and $\epsilon = 0.1$.

In the same figure, the flow streamlines are coloured by the velocity magnitude, in grey colour scale. The qualitative good agreement evinced from figure 5 is quantified in figure 6, where we sample the solution of the upward and downward membrane sides, immediately outside of the potential range. The normal(tangential)-to-the membrane velocity is symmetric (anti-symmetric) with respect to the membrane centreline, while the concentration field presents a sharp jump generated by the source S_i. The macroscopic model (yellow and purple lines) reproduces well the averages (black symbols) of the full-scale solution (black lines). We notice only a discrepancy in the concentration values (figure 6*d*). However, the concentration jump is correctly captured by the macroscopic model with relative error 0.9 %.

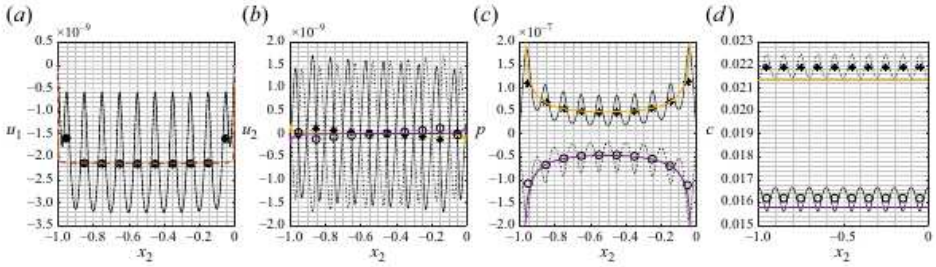

Figure 6. Comparison between the full-scale (pointwise fields black solid, and dashed line for the left- and right-hand sides, respectively; average fields black asterisks, and circles for the left- and right-hand sides of the membrane, respectively) and macroscopic (yellow and purple for the left- and right-hand sides of the membrane, respectively): (*a*,*b*) velocity components, (*c*) pressure and (*d*) solute concentration on the membrane sides when $\theta = 0$ and $\epsilon = 0.1$.

In a second configuration, we modify the source term S by imposing $\theta = \pi/4$ while maintaining the same geometrical properties of the microstructure. In this case, the concentration gradient is not fully normal to the membrane, and a non-zero vertical velocity is generated (figure 7*a*,*b*). The presence of this vertical velocity produces two recirculation regions near the edges of the membrane. These vortices are slightly smaller in the macroscopic simulation. Figure 7(*c*–*f*) show that the flow in the close vicinity of the edges is not periodic. Therefore, while the macroscopic model well reproduces the flow behaviour in the internal part of the membrane, the breakdown of the periodicity near the membrane edges produces slight macroscopic deviations. As concerns the concentration field, the model correctly reproduces the concentration jump across the membrane with relative error approximately 3 %. Despite these small deviations, likely mainly induced by the use of periodic microscopic problems (see e.g. Ledda *et al.* 2021), the model faithfully reproduces the macroscopic behaviour of the flow, including hydrodynamics, transport and phoretic effects, only relying on interface conditions closed by known quantities.

4. Short-range potential limit

In the case of short-range potential ($\lambda \ll \ell$), the effects of the interaction potential ϕ are felt only in the close vicinity of the solid boundary while they can be neglected in the bulk fluid. The governing equations degenerate in a coupled Stokes–Smoluchowski equation without the interaction potential, as in Zampogna *et al.* (2023). However, a boundary layer analysis allows us to embed the interaction potential effects in a phoretic slip boundary condition for the solvent velocity and an effective solute flux at the membrane walls; see Michelin & Lauga (2014) for further details. The full problem hence reads

$$\begin{cases} Re_\ell u_j^{\mathbb{I}}\, \partial_j u_i^{\mathbb{I}} = -\partial_i p^{\mathbb{I}} + \partial_{jj}^2 u_i^{\mathbb{I}}, \\ \partial_i u_i^{\mathbb{I}} = 0, \\ \partial_i F_i^{\mathbb{I}} = 0, \\ F_i^{\mathbb{I}} = Pe_\ell\, u_i^{\mathbb{I}} c^{\mathbb{I}} - D\, \partial_i c^{\mathbb{I}} \\ u_i^{\mathbb{I}} = M\big(\delta_{ij} - n_i^{\mathbb{M}} n_j^{\mathbb{M}}\big)\partial_j c^{\mathbb{I}} \text{ on } \partial\mathbb{M}, \\ c^{\mathbb{I}} = S_i(X)\, n_i^{\mathbb{M}} \text{ on } \partial\mathbb{M}, \end{cases} \tag{4.1}$$

where M is the motility scalar (Michelin & Lauga 2014). The source condition on the solute at the membrane walls $\partial\mathbb{M}$ is specified here in terms of concentration and not in

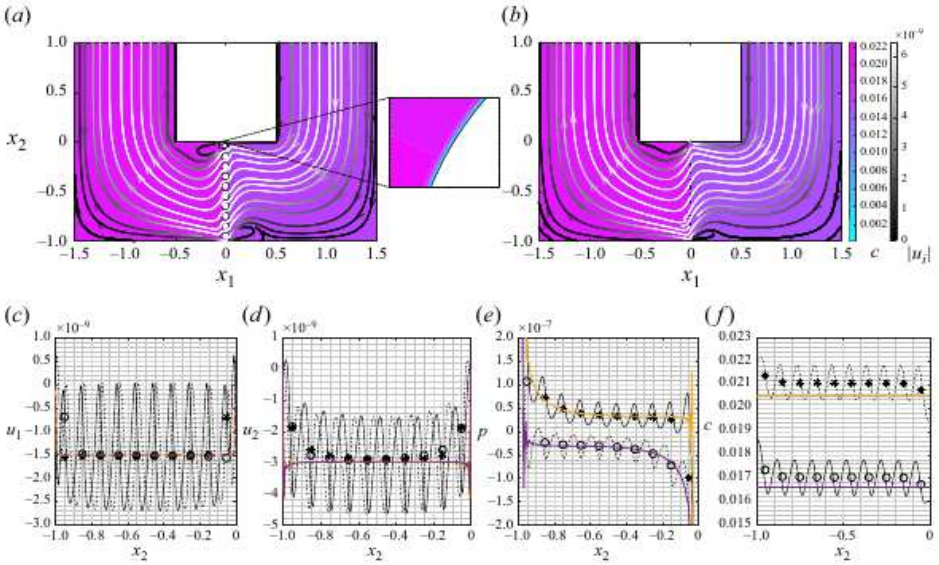

Figure 7. Plots for $\theta = \pi/4$ and $\epsilon = 0.1$. (*a*,*b*) Same as figure 5. (*c*–*f*) Comparison between the full-scale averaged fields (black asterisks and circles for the left- and right-hand sides of the membrane, respectively) and macroscopic (yellow and purple for the left- and right-hand sides of the membrane, respectively) velocity components, pressure, and solute concentration on the membrane.

terms of fluxes. However, one could introduce additional parameters to specify the source as a concentration flux, as already done in Zampogna *et al.* (2023). Applying the same procedure as in § 3, we obtain the following leading-order problem

$$\begin{cases} -\partial_i p^{\mathbb{I},0} + \partial^2_{ll} u_i^{\mathbb{I},0} = 0, \\ \partial_i u_i^{\mathbb{I},0} = 0, \\ \partial_i F_i^{\mathbb{I},0} = 0, \\ F_i^{\mathbb{I},0} = -\partial_i c^{\mathbb{I},0}, \\ u_i^{\mathbb{I},0} = M\left(\delta_{ij} - n_i^{\mathbb{M}} n_j^{\mathbb{M}}\right) \partial_j c^{\mathbb{I},0} \quad \text{on } \partial\mathbb{M}, \\ c^{\mathbb{I},0} = S_i(X)\, n_i^{\mathbb{M}} \text{ on } \partial\mathbb{M}, \end{cases} \tag{4.2}$$

since we assumed that Re_ℓ and Pe_ℓ are of order $\mathcal{O}(\epsilon)$ (Zampogna, Ledda & Gallaire 2022). Following the same steps as in § 3, problem (4.2) is closed by the far-field boundary conditions (3.7) and (3.8) on the sides $\mathbb{U}$ and $\mathbb{D}$ of the microscopic elementary cell, which are not affected by the presence of the interaction potential. Applying averages (3.16) to the formal solution of problem (4.2), adopting the notation introduced in (3.25) and neglecting the superscripts $\mathbb{I}$, 0, we obtain

$$u_i^- = \mathcal{M}_{ij}^- \Sigma_{jk}^{\mathbb{C}^-} n_k + \mathcal{N}_{ij}^- \Sigma_{jk}^{\mathbb{C}^+} n_k + \overline{u_i^{ph}}^-, \tag{4.3}$$

$$u_i^+ = \mathcal{M}_{ij}^+ \Sigma_{jk}^{\mathbb{C}^-} n_k + \mathcal{N}_{ij}^+ \Sigma_{jk}^{\mathbb{C}^+} n_k + \overline{u_i^{ph}}^+, \tag{4.4}$$

$$p^- = \mathcal{Q}_j^- \Sigma_{jk}^{\mathbb{C}^-} n_k + \mathcal{R}_j^- \Sigma_{jk}^{\mathbb{C}^+} n_k + \overline{p^{ph}}^-, \tag{4.5}$$

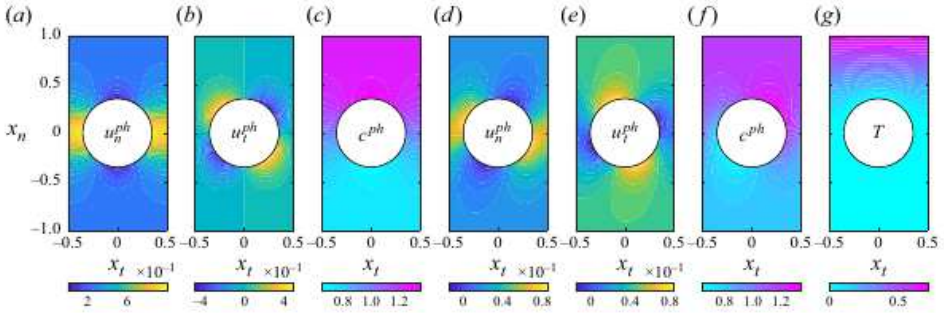

Figure 8. Contours of the microscopic fluid flow-related fields u_n^{ph}, u_t^{ph} and concentration-related fields c^{ph}, T in the case of short-range potential around a circular, solid inclusion for (*a–c*) $\theta = 0$ and (*d–f*) $\theta = \pi/4$, and $C_0 = 1$ in (3.34).

$$p^+ = \mathcal{Q}_j^+ \Sigma_{jk}^{\mathbb{C}^-} n_k + \mathcal{R}_j^+ \Sigma_{jk}^{\mathbb{C}^+} n_k + \overline{p^{ph}}^+, \tag{4.6}$$

$$c^- = \mathcal{T}^- F_k^{\mathbb{C}^-} n_k + \mathcal{Y}^- F_k^{\mathbb{C}^+} n_k + \overline{c^{ph}}^-, \tag{4.7}$$

$$c^+ = \mathcal{T}^+ F_k^{\mathbb{C}^-} n_k + \mathcal{Y}^+ F_k^{\mathbb{C}^+} n_k + \overline{c^{ph}}^+, \tag{4.8}$$

where u_i^{ph}, p^{ph} and c^{ph}, solve the following microscopic problems

$$\begin{cases} -\partial_i p^{ph} + \partial_{ll}^2 u_i^{ph} = 0 \text{ in } \mathbb{F} \\ \partial_i u_i^{ph} = 0 \text{ in } \mathbb{F} \\ u_i^{ph} = M\left(\delta_{ij} - n_i^{\mathbb{M}} n_j^{\mathbb{M}}\right) \partial_j c^{\mathbb{M}} \text{ on } \partial\mathbb{M} \\ \Sigma_{pq}\left(u^{ph}, p^{ph}\right) n_q = 0 \text{ on } \mathbb{U}, \mathbb{D} \\ u_i^{ph},\ p^{ph} \text{ periodic along } \boldsymbol{t}, \boldsymbol{s}, \end{cases} \qquad \begin{cases} \partial_{ii}^2 c^{ph} = 0 \text{ in } \mathbb{F} \\ c^{ph} = S_i(X)\, n_i^{\mathbb{M}} \text{ on } \partial\mathbb{M} \\ \partial_n c^{ph} = 0 \text{ on } \mathbb{U}, \mathbb{D} \\ c^{ph} \text{ periodic along } \boldsymbol{t}, \boldsymbol{s}, \end{cases} \tag{4.9}$$

while tensors M_{ij} and N_{ij} and scalars T and Y solve, respectively, problems (3.12) and (3.13), in which the term involving ϕ disappears, and the boundary condition on $\partial\mathbb{M}$ reduces to $T = Y = 0$. In the short-range potential limit, new quantities p^{ph}, u_i^{ph} and c^{ph} are introduced in place of A_i, B_i, C, D, γ, α_i, η. The effect of the potential is now embedded in two non-homogeneous boundary conditions on $\partial\mathbb{M}$ in problems (4.9). As mentioned at the beginning of the section, the short- and long-range descriptions are equivalent if $\lambda \ll \ell$. However, for a given source term S_i^* in the long-range potential equation, the source term S_i that produces the same solvent and solute behaviour is different from S_i^* since it must embed also the effect of ϕ in the boundary condition on c^{ph}.

4.1. *Microscopic solution*

Problem (3.12) has been analysed in § 3.2.1, and its solution is not affected by the short-range potential hypothesis. Systems (3.13) and (4.9) are solved within the same microscopic geometry described in § 3.2.1, containing a solid circular inclusion of radius 0.35. Fields u_i^{ph}, c^{ph}, T are shown in figure 8, for $\theta = 0$, $C_0 = 1$ in (3.34). As observed in § 3.2.1, the distributions of u_i^{ph} (figure 8*a*,*b*) exhibit maxima at the solid inclusion surface $\partial\mathbb{M}$ since u_i^{ph} represents the velocity contribution due to the diffusio-phoretic mechanisms in the

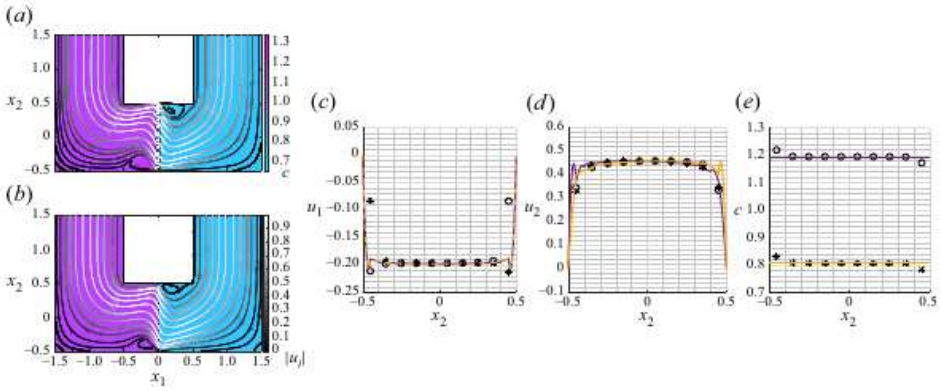

Figure 9. Plots for $\theta = \pi/4$ and $\epsilon = 0.1$. (*a*) Full-scale and (*b*) macroscopic solutions in the U-shaped channel in the case of short-range potential. Contours show the solute concentration values, while streamline colours represent the local velocity magnitude. (*c*,*d*,*e*) Comparison between the full-scale averaged fields (black asterisks and circles for the left- and right-hand sides of the membrane, respectively) and macroscopic (yellow and purple for the left- and right-hand sides of the membrane, respectively) velocity components and solute concentration on the membrane.

vicinity of the membrane walls (figure 8*c*). The chemical slip represents the only inhomogeneous source term in the problem for u_i^{ph}. Since the gradient of c^{ph} is symmetric with respect to the vertical axis x_n, u_n^{ph} and u_t^{ph} are symmetric to the same axis. The solute-related quantity c^{ph} depends on S_i and represents the solute concentration variation at the membrane walls $\partial\mathbb{M}$ imposed via S_i. A change in S_i can modify the symmetry axis of c^{ph} (figure 8*e*), implying a rotation of the maxima in u_i^{ph} and a consequent deviation of the velocity principal direction with respect to the axis x_n. These variations are not present in T, which does not depend on S_i and exhibits a behaviour analogous to the long-range case.

4.2. *Macroscopic solution and comparisons with fully solved simulations*

We compare the short-range potential macroscopic model to full-scale simulations of (4.1) for the same flow configuration of the long-range potential case in § 3 (cf. figure 9*a*,*b*). We consider a membrane whose physio-chemical properties are described by S_i with $\theta = \pi/4$. As evinced by figure 9(*a*,*b*), the fluid flows from right to left and exhibits a non-negligible transversal velocity component at the membrane, induced by a concentration gradient rotated by θ with respect to the membrane centreline. While the velocity field is continuous across the membrane (figure 9*c*,*d*), we observe a sharp concentration jump (figure 9*e*). In figure 9(*c*–*e*), the comparison between the average full-scale velocity components, the solute concentration (black symbols) and the macroscopic solution (coloured lines) shows good agreement.

Therefore, our homogeneous model faithfully reproduces phoretic mechanisms within the membrane in a large range of conditions, from the presence of a chemical interaction potential that varies at the scale of the elementary cell, to the case in which these interactions are confined in the very vicinity of the solid walls. We now conclude our analysis by showing a simple application of the homogenised model.

4.3. *Towards a rational design of minimal phoretic pumps within microchannels*

The generation of a net flow rate and recirculation regions in the inertialess regime without moving parts in microfluidics is a problem of large interest; see e.g. Amselem, Clanet &

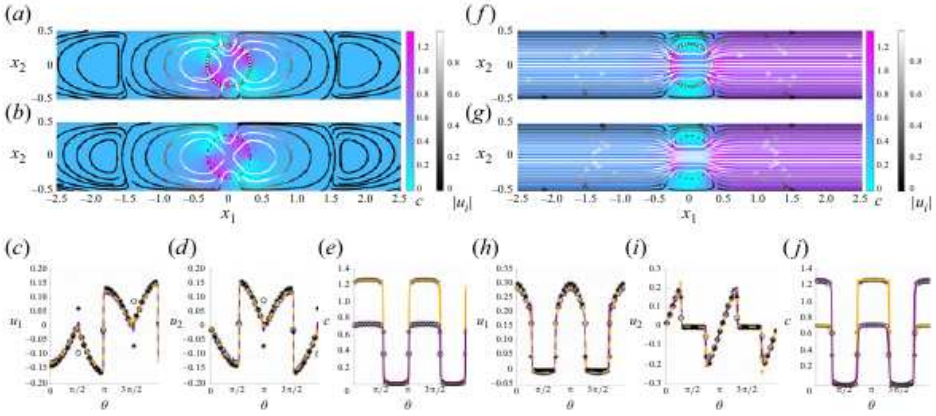

Figure 10. Plots for $(a–e)$ $\theta = 0$ and $(f–j)$ $\theta = \pi/2$. (a,b,f,g) Full-scale and macroscopic concentration c contours and streamlines coloured by velocity magnitude, respectively. $(c–e,h–j)$ Full-scale averaged (black) velocity components and concentration on the inner (asterisks) and outer (circles) and corresponding macroscopic quantities on the inner (yellow) and outer (purple) sides of the membrane.

Benzaquen (2023). As a matter of fact, phoretic mechanisms can be utilised to generate a net flow rate in the absence of valves and moving parts (Tan, Yang & Ripoll 2019). Here, we present a simple design of a minimal phoretic pump to guide an additional passive, inert solute concentration field c^*, similar to the experimental set-up of Lee *et al.* (2014), where an inert solute was employed to visualise the developing flow field. In our case, we consider a simple geometry that consists of a circular membrane immersed in a rectangular two-dimensional channel, which serves also as a further validation test for the model. We set $\epsilon = 0.025$. We introduce a macroscopic angle ψ that identifies the rotation of the circular membrane with respect to $x_1 = 0$ and is measured clockwise. When $\psi = 0$, on the mth solid inclusion, we impose

$$S_i n_i = \frac{1}{\epsilon}\left[\cos(m\pi/20)\left(x + \frac{\cos(n\pi/20)}{\pi}\right) + \sin(m\pi/20)\left(y + \frac{\sin(m\pi/20)}{\pi}\right)\right] + 1 \tag{4.10}$$

if $m \in [1, 6]$, $[16, 26]$ or $[36, 40]$, while for the other values of m, $S_i n_i = 0$. These intervals characterise two regions (leftmost and rightmost portions of the circle) where the source is active, and the other two regions (uppermost and lowermost regions of the circle), where the source term is zero. We note that $m = 1$ corresponds to the leftmost inclusion in figure 10(a), and m increases anticlockwise. At the centre of the circular membrane, a pointwise inlet releases continuously in time a constant concentration of $c^* = 1$, which is then advected by the steady (u_1, u_2) fluid flow field. We assume that the Péclet number of the inert species is $Pe_L^* = (U^{\textcircled{i}} L/D^*) = 1000$, and use the central approximation provided in Zampogna *et al.* (2022) to compute the equivalent diffusivity $T^* = 0.795$ on the homogeneous interface. By rotating the membrane by an angle $\psi \in [0, \pi/2]$, we can generate a net fluid flow or recirculating patterns along the channel; see figure 10. Recirculating patterns are of utmost interest within the low Reynolds number regime since they can enable controlled microfluidic mixing and chemical reactions (Ault, Shin & Stone 2018; Teng, Rallabandi & Ault 2023). In this case, recirculations are generated without the need for pumps, valves and flexible walls or elements. The homogenised model is suitable

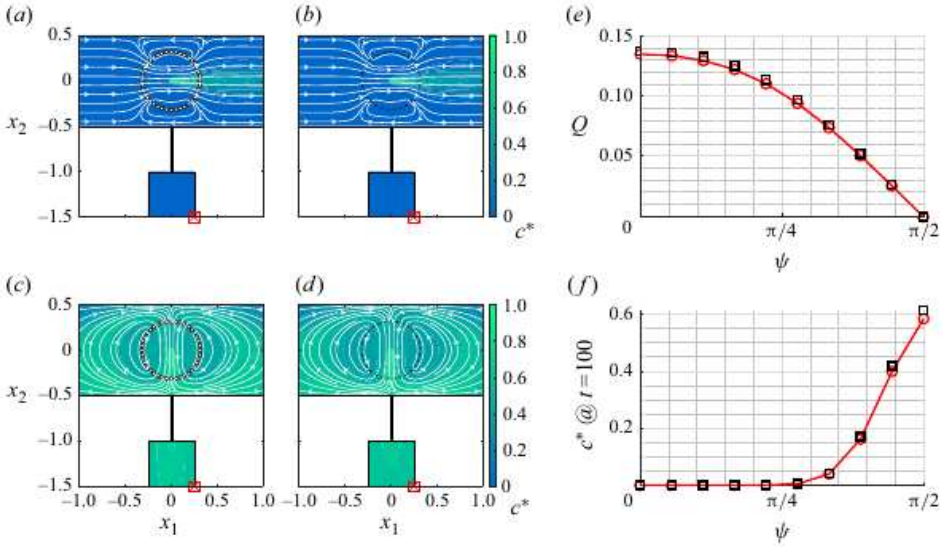

Figure 11. Channel with tank connected in the (a,b) $\theta = 0$ and(c,d) $\theta = \pi/2$ cases. $(a–d)$ Iso-levels of inert concentration c^* in the (a,c) full scale and (b,d) macroscopic solutions at $\tau = 100$. Velocity streamlines in white. The red cross indicates the location of the concentration probe used in (f). (e,f) The flow rate $Q = \int_{-0.5}^{0.5} u_i n_i \, \mathrm{d}x_2$ and the inert concentration at the probe for $\tau = 100$, respectively.

for a fine-tuning of the properties of the membrane and a subsequent inverse design approach to retrieve these values; see e.g. Ledda *et al.* (2021) for the hydrodynamic case.

In addition to these considerations, we include in the analysis a tank with a small connection on the side of the channel, as shown in figure 11$(a–d)$. We simulate the filling of the tank with a required concentration of inert solute c^* by monitoring its evolution in time $\tau = t/T^{\mathbb{O}} \in [0, 100]$, where $T^{\mathbb{O}}$ is the macroscopic time scale defined above as $T^{\mathbb{O}} = L/U^{\mathbb{O}}$ for a range of θ. The flow rate and concentration at the tank corner marked in red are shown in figure 11(e,f). By changing the direction of the source term on the membrane, we are not only creating a phoretic pump, but can also selectively guide the inert concentration to achieve a desired local concentration at some point in the domain. The full-scale and macroscopic simulations agree well on these trends. This final application demonstrates how the homogenisation technique proposed in this paper can be used even in the presence of macroscopic unsteadiness and a third, inert, species. The model allows for a cost-effective computation of phoretic flows across thin, porous membranes, in the case of both long- and short-range potentials. An indirect computational advantage of this technique resides in the absence of stiff regions in the macroscopic simulation: indeed, in the full-scale simulation, the local grid refinement on each solid inclusion must account for steep variations of the potential, which may generate grids with high expansion ratios. Moreover, the method allows for the exploration of various geometry and source/potential configurations by only modifying terms in the microscopic problems, offering interesting perspectives for membrane design applications.

5. Conclusion and outlooks

We developed a model to describe the diffusio-phoretic transport across microstructured surfaces, fully permeable to the solute. The model is fully closed, i.e. it does not rely on

any fitting parameter except the shape of the potential ϕ once chemical and hydrodynamic properties are known. The model accounts for the presence of the microstructure via a macroscopic condition on the variables imposed on a smooth single-scale interface without thickness between two fluid regions. As a matter of fact, quantities across the membrane are discontinuous due to chemical interactions at the pore scale.

We considered and validated against full-scale simulations two different levels of approximation at the microscopic scale, where the chemical potential variations (i) propagate into the elementary cell of the membrane, and (ii) are felt only in the vicinity of the solid pores, the latter case allowing for a boundary-condition-based description also at the microscale. These characterisations of chemically enabled flows in the vicinity of solid interacting walls have already been employed in the literature, e.g. by Michelin & Lauga (2014) and Marbach, Yoshida & Bocquet (2017). The short-scale approximation appears as a viable method to consider the leading-order chemical interactions in the vicinity of the solid walls.

From a macroscopic point of view, the velocity and the concentration are described by a linear combination of the upward and downward stress tensors and solute fluxes, and some source terms that represent the upscaled phoretic contribution to the flow, deriving from the solute–solvent–membrane interactions. Quantities present in the macroscopic condition are the averaged entries of tensors retrieved by the solution of Stokes–Smoluchowski problems with a potential source term, within a periodic microscopic domain. The phoretic contributions to the flow macroscopically result in a net flow and concentration source at the membrane, which depends on the chemical interaction on the solid boundaries of the microscopic inclusions composing the membrane.

The model shows a high degree of generality as concerns (i) the microscopic topology of the membrane (only periodicity along the tangential to the surface direction is imposed), and (ii) the macroscopic shape of the membrane (whose unique constraint is the separation of scales $l/L = \epsilon \ll 1$). Furthermore, the condition applies to generic flow configurations involving chemical and electrical interactions embedded within a specified interaction potential as well as to different chemical interactions between solid boundaries and fluid flow, thus suggesting promising applications in the modelling of phoretic mechanisms, such as pumping and recirculating effects for microfluidics systems, as discussed in a dedicated example.

It is worth mentioning some limits of the model here.

First, the model applies when the pore size is such that continuum Stokes–Smoluchowski equations are valid (cf. for instance, filtration processes such as industrial wastewater treatment, and water reuse involving membranes whose pore diameter is larger than a few nanometres; Kirby 2010). Important biological processes happen at smaller scales, across sub-nanometric pores (cf. for instance, Verkman 2012). Indeed, membranes are typically geometrically selective, i.e. they do not allow solute particles and ions beyond a certain size to pass through the membrane. Our model does not contain such geometrical ingredient, resulting in a partial membrane permeability to the solute. For this reason, the accumulation of chemical species on the membrane (i.e. fouling and concentration polarisation) is not currently modelled in the proposed framework. This ingredient involves the introduction of more refined microscopic descriptions to account for confinement effects (Gravelle *et al.* 2013), such as the employment of space varying solvent density and viscosity or solute diffusivity.

Second, the model here presented is developed only for one transported species. However, in the limit of non-interacting diluted solutes of different species, the model can be straightforwardly generalised to several species thanks to the linear superposition principle. This task has partially been fulfilled in § 4.3, when an inert (i.e. interacting

neither with other solutes nor with the membrane) species was advected by the diffusiophoretic flow. In the long-range case, we would have

$$u_i^{\pm} = \epsilon \overline{M}_{ij}^{\mathbb{C}^{\pm}} \Sigma_{jk}^{\pm} n_k + \epsilon \overline{N}_{ij}^{\mathbb{C}^{\pm}} \Sigma_{jk}^{\mp} n_k + \epsilon^2 \sum_{n=1}^{n_{sp}} \left(\overline{A}_i^{(n),\mathbb{C}^{\pm}} F_k^{(n),\pm} n_k + \epsilon \overline{B}_i^{(n),\mathbb{C}^{\pm}} F_k^{(n),\mp} n_k + \epsilon \overline{\alpha}_i^{(n),\mathbb{C}^{\pm}} \right), \tag{5.1}$$

$$c^{(n),\pm} = \epsilon \left(\overline{T}^{(n),\mathbb{C}^{\pm}} F_k^{(n),\mp} n_k + \overline{Y}^{(n),\mathbb{C}^{\pm}} F_k^{(n),\pm} n_k + \overline{\gamma}^{(n),\mathbb{C}^{\pm}} \right), \tag{5.2}$$

and in the short-range case,

$$u_i^{\pm} = \epsilon \overline{M}_{ij}^{\mathbb{C}^{\pm}} \Sigma_{jk}^{\pm} n_k + \epsilon \overline{N}_{ij}^{\mathbb{C}^{\pm}} \Sigma_{jk}^{\mp} n_k + \epsilon^2 \sum_{n=1}^{n_{sp}} \left(\epsilon \overline{u_i^{ph}}^{(n),\mathbb{C}^{\pm}} \right), \tag{5.3}$$

$$c^{(n),\pm} = \epsilon \left(\overline{T}^{(n),\mathbb{C}^{\pm}} F_k^{(n),\mp} n_k + \overline{Y}^{(n),\mathbb{C}^{\pm}} F_k^{(n),\pm} n_k + \overline{c^{ph}}^{(n),\mathbb{C}^{\pm}} \right), \tag{5.4}$$

where each term $\cdot^{(n)}$ stems from the previously derived Smoluchowski-like problems for each chemical potential and boundary conditions associated with each solute.

A further extension, to close the gap towards modelling of actual complex biological systems, such as the flow through the retinal epithelium (Dvoriashyna *et al.* 2020), would be to include the chemical reactions between different solutes within a similar general, rigorous and closed model. For example, Boso & Battiato (2013) applied homogenisation to multi-component reactive species in bulk porous media.

Third, the model assumes that convective terms within the governing equations can be neglected, i.e. $Re_\ell, Pe_\ell \ll 1$. Further developments could relax the hypothesis by including an Oseen-like approximation (Zampogna *et al.* 2016; Wittkowski *et al.* 2024) to extend the range of validity of the current model toward larger scales, or different solute–solvent interaction regimes. This would enable the presence of the solvent fluid stresses in the interface conditions (3.21) and (3.22) for the solute concentration, leading hence to a fully coupled transport dynamics in agreement with the Onsager reciprocal relations of thermodynamics (Onsager 1931).

In summary, we have proposed a rigorous and closed model to describe transport across phoretic membranes. In addition to the good predictive power combined with significantly reduced computational times, the model is potentially suitable for optimisation and inverse design procedures; see Ledda *et al.* (2021). We envisage this model to be employed as a building block towards an improved physical understanding of interfacial transport across biological and engineered membranes for innovative applications, as well as for the actual design of phoretic systems for net transport and mixing of solutes within microfluidic devices and beyond.

Funding. This work was supported by the Swiss National Science Foundation (grant no. PZ00P2_193180) and by the Italian Ministry of the University and Research via the 'Rita Levi Montalcini' grant to G.A.Z. (D.M. n. 1317, 15/12/2021, published on GU Serie Generale n. 226, 27/09/2022).

Declaration of interests. The authors report no conflict of interest.

Appendix A. Mesh independence study

In this appendix, we assess the robustness of the results with respect to the mesh size. As a test case, we consider the long-range case. As a matter of fact, the presence of a boundary layer in the vicinity of the solid walls due to the functional form of potential ϕ is

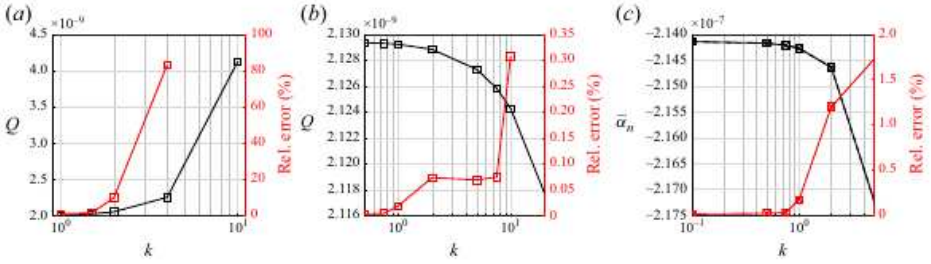

Figure 12. Flow rate Q (black lines) evolving in the U-shaped pipe in (a) the full-scale simulation and (b) the macroscopic simulation as a function of the mesh factor k. The corresponding relative error is shown on the right-hand vertical axis (red). Frame (c): average values of α_n (black) as a function of the mesh factor k. Corresponding relative errors are shown on the left vertical axis (red).

computationally more challenging than the short-range case, where the interaction appears as a boundary condition. The parameters of the initial grid are as follows.

(i) For the full-scale computation (the reference set-up is shown in figure 7a): overall maximum mesh size $0.05L$, maximum element size near the solid inclusions $0.00038L$, with first cell height of the prismatic layers $6.25 \times 10^{-6}L$.
(ii) For the macroscopic computation (the reference set-up is shown in figure 7b): overall maximum mesh size $0.1L$, maximum element size near the solid inclusions $0.001L$.
(iii) For the microscopic computation (corresponding to figure 3): overall maximum mesh size 0.02ℓ, maximum element size near the solid inclusions 0.001ℓ.

All these mesh parameters except the overall sizing were perturbed by multiplying them by a factor k, and computing a solution for each k. Figure 12 shows that for $k = 1$ in all cases, we can expect an error of order

(i) 1.0 % on the flow rate Q evolving in the system for the full-scale simulation
(ii) 0.018 % on the flow rate Q evolving in the system for the macroscopic simulation
(iii) 0.17 % on the values of $\bar{\alpha}_n$ for the microscopic simulation.

Meshes with $k = 1$ have been employed for all calculations performed in this work.

References

Adler, J. 1975 Chemotaxis in bacteria. *Annu. Rev. Biochem.* **44** (1), 341–356.

Amselem, G., Clanet, C. & Benzaquen, M. 2023 Valveless pumping at low Reynolds numbers. *Phys. Rev. Appl.* **19** (2), 024017.

Anderson, J.L. 1989 Colloid transport by interfacial forces. *Annu. Rev. Fluid Mech.* **21** (1), 61–99.

Anwar, T. & Tagliabue, G. 2024 Salinity-dependent interfacial phenomena toward hydrovoltaic device optimization. *Device* **2** (5), 100287.

Ault, J.T., Shin, S. & Stone, H.A. 2018 Diffusiophoresis in narrow channel flows. *J. Fluid Mech.* **854**, 420–448.

Bohr, T., Rademaker, H. & Schulz, A. 2018 *Water Motion and Sugar Translocation in Leaves*. Springer International Publishing.

Boso, F. & Battiato, I. 2013 Homogenizability conditions for multicomponent reactive transport. *Adv. Water Resour.* **62**, 254–265.

Brady, J.F. 2021 Phoretic motion in active matter. *J. Fluid Mech.* **922**, A10.

Cardoso, S.S.S. & Cartwright, J.H.E. 2014 Dynamics of osmosis in a porous medium. *Roy. Soc. Open Sci.* **1** (140352)

CHEN, L., TU, B., LU, X., LI, F., JIANG, L., ANTONIETTI, M. & XIAO, K. 2021 Unidirectional ion transport in nanoporous carbon membranes with a hierarchical pore architecture. *Nat. Commun.* **12**, 4650.

LA COUR, M. & TEZEL, T. 2005 The retinal pigment epithelium. *Adv. Organ Biol.* **10**, 253–272.

DERJAGUIN, B.V., SIDORENKOV, G.P., ZUBASHCHENKOV, E.A. & KISELEVA, E.V. 1947 Kinetic phenomena in boundary films of liquids. *Colloid J. USSR* **9**, 335–347.

DVORIASHYNA, M., FOSS, A.J.E., GAFFNEY, E.A., JENSEN, O.E. & REPETTO, R. 2018 Osmotic and electroosmotic fluid transport across the retinal pigment epithelium: a mathematical model. *J. Theor. Biol.* **456**, 233–248.

DVORIASHYNA, M., FOSS, A.J.E., GAFFNEY, E.A. & REPETTO, R. 2020 Fluid and solute transport across the retinal pigment epithelium: a theoretical model. *J. R. Soc. Interface* **17** (163), 20190735.

ELIMELECH, M., GREGORY, J., JIA, X. & WILLIAMS, R.A. 1995 Surface interaction potentials. In *Particle Deposition and Aggregation*, (ed. M. ELIMELECH, J. GREGORY, X. JIA & R.A. WILLIAMS), pp. 33–67. Butterworth-Heinemann.

GEBÄCK, T. & HEINTZ, A. 2019 A pore scale model for osmotic flow: homogenization and lattice Boltzmann simulations. *Transp. Porous Med.* **126**, 161–176.

GRAVELLE, S., JOLY, L., DETCHEVERRY, F., YBERT, C., COTTIN-BIZONNE, C. & BOCQUET, L. 2013 Optimizing water permeability through the hourglass shape of aquaporins. *Proc. Natl Acad. Sci. USA* **110** (41), 16367–16372.

HERMAN, A. & SEGEV, G. 2024 Ambipolar ion pumping with ratchet-driven active membranes. *Phys. Rev. Appl.* **21**, 034056.

HOWSE, J.R., JONES, R.A., RYAN, A.J., GOUGH, T., VAFABAKHSH, R. & GOLESTANIAN, R. 2007 Self-motile colloidal particles: from directed propulsion to random walk. *Phys. Rev. Lett.* **99** (4), 048102.

JENSEN, K.H., BERG-SØRENSEN, K., BRUUS, H., HOLBROOK, N.M., LIESCHE, J., SCHULZ, A., ZWIENIECKI, M.A. & BOHR, T. 2016 Sap flow and sugar transport in plants. *Rev. Mod. Phys.* **88** (3), 035007.

JIMÉNEZ BOLAÑOS, S. & VERNESCU, B. 2017 Derivation of the navier slip and slip length for viscous flows over a rough boundary. *Phys. Fluids* **29** (057103)

KEDEM, O. & KATCHALSKY, A. 1958 Thermodynamic analysis of the permeability of biological membranes to non-electrolytes. *Biochimica et Biophysica Acta* **27**, 229–246.

KIRBY, B.J. 2010 *Micro- and Nanoscale Fluid Mechanics: Transport in Microfluidic Devices*. Cambridge University Press.

KOTER, S. 2006 Determination of the parameters of the Spiegler–Kedem–Katchalsky model for nanofiltration of single electrolyte solutions. *Desalination* **198** (1), 335–345.

LEDDA, P.G., BOUJO, E., CAMARRI, S., GALLAIRE, F. & ZAMPOGNA, G.A. 2021 Homogenization-based design of microstructured membranes: wake flows past permeable shells. *J. Fluid Mech.* **927**, A31.

LEE, C., COTTIN-BIZONNE, C., BIANCE, A.-L., JOSEPH, P., BOCQUET, L. & YBERT, C. 2014 Osmotic flow through fully permeable nanochannels. *Phys. Rev. Lett.* **112**, 244501.

LI, S.R., HUO, F.Y., WANG, H.Q., WANG, J., XU, C., LIU, B. & BU, L.L. 2022 Recent advances in porous nanomaterials-based drug delivery systems for cancer immunotherapy. *J. Nanobiotechnology* **20**, 277.

MALONE, G.H., HUTCHINSON, T.E. & PRAGER, S. 1974 Molecular models for permeation through thin membranes: the effect of hydrodynamic interaction on permeability. *J. Fluid Mech.* **65** (4), 753–767.

MARBACH, S., YOSHIDA, H. & BOCQUET, L. 2017 Osmotic and diffusio-osmotic flow generation at high solute concentration. I. Mechanical approaches. *J. Chem. Phys.* **146** (19), 194701.

MEI, C.C. & VERNESCU, B. 2010 *Homogenization Methods for Multiscale Mechanics*. World Scientific.

MICHELIN, S. & LAUGA, E. 2014 Phoretic self-propulsion at finite Péclet numbers. *J. Fluid Mech.* **747**, 572–604.

MICHELIN, S. & LAUGA, E. 2019 Universal optimal geometry of minimal phoretic pumps. *Sci. Rep. UK* **9** (1), 1–7.

MICHELIN, S., MONTENEGRO-JOHNSON, T.D., DE CANIO, G., LOBATO-DAUZIER, N. & LAUGA, E. 2015 Geometric pumping in autophoretic channels. *Soft Matt.* **11** (29), 5804–5811.

ONSAGER, L. 1931 Reciprocal relations in irreversible processes I. *Phys. Rev.* **37**, 405–426.

PALACCI, J., ABÉCASSIS, B., COTTIN-BIZONNE, C., YBERT, C. & BOCQUET, L. 2010 Colloidal motility and pattern formation under rectified diffusiophoresis. *Phys. Rev. Lett.* **104**, 138302.

PALACCI, J., SACANNA, S., STEINBERG, A.P., PINE, D.J. & CHAIKIN, P.M. 2013 Living crystals of light-activated colloidal surfers. *Science* **339** (6122), 936–940.

PAXTON, W.F., KISTLER, K.C., OLMEDA, C.C., SEN, A., ST. ANGELO, S.K., CAO, Y., MALLOUK, T.E., LAMMERT, P.E. & CRESPI, V.H. 2004 Catalytic nanomotors: autonomous movement of striped nanorods. *J. Am. Chem. Soc.* **126** (41), 13424–13431.

PEETERS, J.M.M., BOOM, J.P., MULDER, M.H.V. & STRATHMANN, H. 1998 Retention measurements of nanofiltration membranes with electrolyte solutions. *J. Membr. Sci.* **145**, 199.

PENG, Z., ZHOU, T. & BRADY, J.F. 2022 Activity-induced propulsion of a vesicle. *J. Fluid Mech.* **942**, A32.

SAFFMAN, P.G. 1960 Dispersion due to molecular diffusion and macroscopic mixing in flow through a network of capillaries. *J. Fluid Mech.* **7** (2), 194–208.

SHARMA, R.K. & EHINGER, B.E.J. 2003 Development and structure of the retina. In *Adler's Physiology of the Eye: Clinical Applications*, vol. **10**, pp. 319–347. Mosby, St. Louis.

SPIEGLER, K.S. & KEDEM, O. 1966 Thermodynamics of hyperfiltration (reverse osmosis): criteria for efficient membranes. *Desalination* **1** (4), 311–326.

TAN, Z., YANG, M. & RIPOLL, M. 2019 Microfluidic pump driven by anisotropic phoresis. *Phys. Rev. Appl.* **11** (5), 054004.

TENG, J., RALLABANDI, B. & AULT, J.T. 2023 Diffusioosmotic dispersion of solute in a long narrow channel. *J. Fluid Mech.* **977**, A5.

THEURKAUFF, I., COTTIN-BIZONNE, C., PALACCI, J., YBERT, C. & BOCQUET, L. 2012 Dynamic clustering in active colloidal suspensions with chemical signaling. *Phys. Rev. Lett.* **108**, 268303.

VERAN, S., ASPA, Y. & QUINTARD, M. 2009 Effective boundary conditions for rough reactive walls in laminar boundary layers. *Intl J. Heat Mass Transfer* **52**, 3712–3725.

VERKMAN, A.S. 2012 Aquaporins in clinical medicine. *Annu. Rev. Med.* **63**, 303–316.

WERBER, J.R., OSUJI, C.O. & ELIMELECH, M. 2016 Materials for next-generation desalination and water purification membranes. *Nat. Rev. Mater.* **1** (5), 1–15.

WHITAKER, S. 1998 *The Method of Volume Averaging*. Springer Science + Business Media.

WHITESIDES, G.M. 2006 The origins and the future of microfluidics. *Nature* **442** (7101), 368–373.

WITTKOWSKI, K., PONTE, A., LEDDA, P.G. & ZAMPOGNA, G.A. 2024 Quasi-linear homogenization for large-inertia laminar transport across permeable membranes. *J. Fluid Mech.* **1000**, A46.

WOOD, B.D., QUINTARD, M. & WHITAKER, S. 2004 Estimation of adsorption rate coefficients based on the Smoluchowski equation. *Chem. Engng Sci.* **59** (10), 1905–1921.

YANG, H.-C., HOU, J., CHEN, V. & XU, Z.-K. 2016 Janus membranes: exploring duality for advanced separation. *Angew. Chem. Intl Ed. Engl.* **55** (43), 13398–13407.

YOSHIDA, K., SATO, T., EOM, S.I., KIM, J.-W. & YOKOTA, S. 2017 A study on an AC electroosmotic micropump using a square pole – slit electrode array. *Sensors Actuators A: Physical* **265**, 152–160.

YU, T., ATHANASSIADIS, A.G., POPESCU, M.N., CHIKKADI, V., GÄTH, A., SINGH, D.P., QIU, T. & FISCHER, P. 2020 Microchannels with self-pumping walls. *ACS Nano* **14** (10), 13673–13680.

ZAMPOGNA, G.A. & GALLAIRE, F. 2020 Effective stress jump across membranes. *J. Fluid Mech.* **892**, A9.

ZAMPOGNA, G.A., LEDDA, P.G. & GALLAIRE, F. 2022 Transport across thin membranes: effective solute flux jump. *Phys. Fluids* **34** (8), 083113.

ZAMPOGNA, G.A., LEDDA, P.G., WITTKOWSKI, K. & GALLAIRE, F. 2023 Homogenization theory captures macroscopic flow discontinuities across janus membranes. *J. Fluid Mech.* **970**, A39.

ZAMPOGNA, G.A., PLUVINAGE, F., KOURTA, A. & BOTTARO, A. 2016 Instability of canopy flows. *Water Resour. Res.* **52** (7), 5421–5432.